Ultrafast –femtosecond-time-resolved chemistry

In this experiment we will introduce the basic pulsed-laser tools for time-resolved studies of femtosecond dynamics in processes of paramount interest in chemistry. The femtosecond time scale includes some slower electronic processes and covers most of molecular nuclear dynamic processes, such as various rovibrations, which also extend into picosecond and longer scale region.

Femtosecond pulses can be used directly as agents or as spectroscopic monitoring tools for photo-excited charge carriers, dynamics of solvation, etc. just to mentation a few. Of particular interest in very fast edge of this scale (going to the atto-scale) are interactions between coherently excited electronic states in fast EM fields.

We will start with experiment first and do the analysis later. The key experiment done here is a basic pulse-pulse (auto)correlation experiment, which measures physical observables of electromagnetic femtosecond scale pulse(s). We will use a new laser LIBRA which operates at ~1kHz, and produces femtosecond pulses in 800nm region at or less than 100fs.

During the lecture and workshop we will develop methods for modeling fast pulses and describe their interaction with some molecular objects. Some Mathematica application templates for analysis of correlation functions will be used for that. We will also learn more about the femto-lasers we use in our experiment (TiS) and molecular physics/photonics of electromagnetic filed interactions.

After becoming familiar with the time measurements tools (experiment below), you will participate in a workshop where you will write a proposal for a project that applies the so called pump-probe experimental architecture. The ultrafast pump-probe method is based on the detection of the laser pulse probe or its effects. For example we can use a well-defined pulse to excite a molecular system into a specific electronic state and then several femtoseconds later probe that state with another pulse, well defined for a process that involves that excited state, say for example its ionization. Note that probe may or may not be energetically or impulse intensity softer than the pump probe. We can vary the time delay between the pump and probe and see how it changes the system response. As we did in other experiments, like other pulse (scattering) response measurements -say DLS, we can invoke help of very small-change-sensitive detection techniques based on auto- or cross- correlations. As always function transform or some learning (AI) techniques could help too.

When the pump probe project is approved we will construct an new experimental configuration for data acquisition and use a similar correlation method for time resolved measurement of a chemical process.

Time measurement-The experimental steps include

– **SAFETY FIRST: Optical glasses MUST be on all the time in the lab. In case of any accident with injuries to body call 911.** Safety procedures (including appropriate optical glassware with relevant OD>7 in the laser regions). Note that pulsed lasers compress high level of energy for a very very short time. These energies may be compared not only to chemical bonds but also to the energies present at astrophysical or radioactive-nuclear events. Damages are instantaneous and permanent. Consequently only small groups of students will work in a controlled environment. You will enter and use only the designated areas of the laboratory room 237 around the autocorrelation instrument setup. You must limit your movement so that you do not disturb the alignment nor cross the laser beam. You must keep your head always above the laser light planes.

-INTRODUCTION TO INSTRUMENTATION: You will firstly prepare and test alignments and properties of autocorrelation (AC) instrument using a less energetic HeNe laser in lab 104 or 301. You will also carefully examine the same prepared AC instrument using the femtosecond pulses. There will be a long ~2m black anodized 1 inch diameter aluminum tube that will bring the laser light to the optical table where the AC system is positioned. DO NOT move or walk close to that tube!

EXPERIMENT: Your first goal is to project the details of the light paths on the drawing or image of the AC system. You mast name and identify all optical and other parts of the system.

You will describe in situ the operation of the system you see and take notes about it. Concepts like coherence, autocorrelation function, SHG, BBO, NDF OD, PD, etc. will be included in your notes.

You will describe the 4 major stapes of the beam alignment from the optical table where the femtosecond pulsed laser is positioned to the AC table, and the AC system alignment. Note that optics for ultrafast spectroscopy is different from regular optics, it is very expensive and requires careful treatment (including special clean gloves). The optics is from a professional research system used at a National Lab. The experiment uses computer controlled micrometer precision driver. The core of AC alignment requires a lot of practice and skills, so please do not disturb it manually unless you have practiced the manual alignment. We will give you precise instructions *in situ* (*on the fly*). - Violation of any procedure steps could result in accidents and damages of you or instrument and you not being able to complete experiment (and could lead to lower grade) .

You will become familiar with the detector and electronics, and the basics of the LaView program and interface (DAQ) that links the detector. You will also go through the procedure for correlation based time measurement.

Finally you will acquire data for the determination of the time of a pulse that will be constructed in the laser compressor specially for you.

After the experiment you will fit the results into a an autocorrelation function and calculate the time in femtoseconds.

Based on the workshop , labnotes, data and calculation you will complete a short report.

x-ray ranges through highly nonlinear harmonic generation processes or by pumping x-ray lasers. Coherent short-wavelength radiation may be important, for example, for imaging microscopic structures such as DNA.

Optical Communications The low-loss transmission window of optical fibers has a bandwidth comparable to that of a 100-fs pulse, and therefore ultrashort-pulse technology may play an important role in optical communications. Subpicosecond pulses have already been used for laboratory experiments demonstrating fiber optic transmission of data at Tbit/s (10^{12} bit/s) rates. Here ultrafast optics technology is important not only for pulse generation but also for signal processing, for data detection, and for the advanced metrology necessary for characterizing and optimizing ultrashort-pulse transmission [3,4]. Ultrashort pulses may also prove important in wavelength-division-multiplexing (WDM) systems in which the fiber bandwidth is carved up into different wavelength bands or channels. For WDM applications it is the large bandwidth of the ultrashort pulse (not the short duration) which is useful, since a single pulse contains enough bandwidth to produce a number of wavelength channels.

Biomedical Applications Ultrashort pulses are finding substantial applications in biomedical imaging. Attractive features include the ability to perform optical imaging within scattering media (e.g., most tissues) and to obtain high-resolution depth information. An example of such an application is discussed in Section 3.3.3. In confocal microscopy significantly improved spatial resolution has been demonstrated by relying on two-photon excitation. The ability of ultrashort pulses to provide high intensity without high pulse energy is important in the use of this technique with sensitive biological samples. In laser-assisted surgical procedures ultrashort pulses may in some cases reduce collateral tissue damage by reducing heat deposition.

Materials Processing High-power lasers are used for a variety of industrial applications, such as cutting and drilling. With continuous-wave or "long"-pulse (nanoseconds) lasers, the minimum feature size and the quality of the cut are limited by thermal diffusion of heat to areas neighboring the laser focus. With femtosecond lasers, materials processing is possible using lower pulse energies, due to the very high peak powers, which lead to new physical mechanisms. This reduces the heat deposited into the sample during the laser machining process and leads to a much cleaner cutting or drilling operation.

1.2 BRIEF REVIEW OF ELECTROMAGNETICS

Since ultrashort laser pulses are made up of light, and light is a form of electromagnetic radiation, we very briefly review Maxwell's equations, which describe all forms of electromagnetic radiation, including light. We use MKS (SI) units here and throughout the book. It is assumed that the reader is already familiar with vector calculus. For a more detailed treatment of electromagnetics, the reader is directed to textbooks on this subject [5,6].

1.2.1 Maxwell's Equations

Maxwell's equations are a set of relationships between the electric field **E** and magnetic field **H** (boldface symbols denote vectors). Inside a medium we must also consider the

Table 1.1 Names and Units of Symbols in Maxwell's Equations

Symbol	Name	Units or Numerical Value
$\mathbf{E}$	Electric field	$\mathrm{V\,m^{-1}}$
$\mathbf{D}$	Electric flux density	$\mathrm{C\,m^{-2}}$
$\mathbf{H}$	Magnetic field	$\mathrm{A\,m^{-1}}$
$\mathbf{B}$	Magnetic flux density	T (or $\mathrm{V{\cdot}s\,m^{-2}}$)
$\mathbf{P}$	Polarization density	$\mathrm{C\,m^{-2}}$
$\mathbf{M}$	Magnetization density	$\mathrm{A\,m^{-1}}$
$\mathbf{J}$	Current density	$\mathrm{A\,m^{-2}}$
ρ	Charge density	$\mathrm{C\,m^{-3}}$
ε_0	Permittivity of free space	$8.85 \times 10^{-12}\ \mathrm{F\,m^{-1}}$ (or $\mathrm{C\,V^{-1}\,m^{-1}}$)
μ_0	Permeability of free space	$4\pi \times 10^{-7}\ \mathrm{H\,m^{-1}}$ (or $\mathrm{V\,s^2\,m^{-1}\,C^{-1}}$)

charge density ρ, current density $\mathbf{J}$, polarization density $\mathbf{P}$, and magnetization density $\mathbf{M}$, and in order to include the effect of the fields on the matter, the electric and magnetic flux densities, $\mathbf{D}$ and $\mathbf{B}$, are also introduced. Units for these quantities are given in Table 1.1. Maxwell's equations are then written as follows:

$$\nabla \cdot \mathbf{D} = \rho \tag{1.1}$$

$$\nabla \cdot \mathbf{B} = 0 \tag{1.2}$$

$$\nabla \times \mathbf{E} = \frac{-\partial \mathbf{B}}{\partial t} \tag{1.3}$$

$$\nabla \times \mathbf{H} = \mathbf{J} + \frac{\partial \mathbf{D}}{\partial t} \tag{1.4}$$

The relations defining $\mathbf{D}$ and $\mathbf{B}$ are

$$\mathbf{D} = \varepsilon_0 \mathbf{E} + \mathbf{P} \tag{1.5}$$

$$\mathbf{B} = \mu_0 (\mathbf{H} + \mathbf{M}) \tag{1.6}$$

The constants ε_0 and μ_0 are known as the *permittivity* and *permeability* of free space, with the numerical values and units given in Table 1.1. Note also that the symbol ρ refers to the free charge density (i.e., any bound charge density associated with the polarization is not included). Similarly, the current density $\mathbf{J}$ does not include any currents associated with the motion of bound charges (changes in polarization). In free space we would have $\rho = \mathbf{J} = \mathbf{P} = \mathbf{M} = 0$.

For now we specialize to the case of a linear, isotropic, and source-free medium. By *source-free* we mean that the charge and current densities are zero ($\rho = 0$ and $\mathbf{J} = 0$). By *linear* we mean that the medium response (i.e., the polarization and magnetization) is linear in the applied fields. For the case of the electric field, we write

$$\mathbf{P} = \varepsilon_0 \chi_e \mathbf{E} \tag{1.7}$$

where χ_e is known as the electric susceptibility (dimensionless). Inserting into eq. (1.5), one obtains

$$\mathbf{D} = \varepsilon_0(1 + \chi_e)\mathbf{E} = \varepsilon\mathbf{E} \tag{1.8}$$

The proportionality constant ε is termed the dielectric constant, with

$$\varepsilon = (1 + \chi_e)\,\varepsilon_0 \tag{1.9}$$

Other common terms include the relative dielectric constant $(\varepsilon/\varepsilon_0)$ and the index of refraction n, which is commonly used in optics, where

$$n^2 = \frac{\varepsilon}{\varepsilon_0} \tag{1.10}$$

For the case of the magnetic field, we write

$$M = \chi_m H \tag{1.11}$$

where χ_m is the magnetic polarizability. Using eq. (1.6), we obtain

$$\mathbf{B} = \mu_0\,(1 + \chi_m)\mathbf{H} = \mu\mathbf{H} \tag{1.12}$$

In most cases in ultrafast optics, one is interested in nonmagnetic materials, for which $\mathbf{M} = 0$. In this case of zero magnetization, one has

$$\mathbf{B} = \mu_0\mathbf{H} \tag{1.13}$$

Equations (1.7) and (1.11) are examples of constitutive laws, which specify the response of the material to the fields. The form of these equations as written arises because we have assumed both linear and isotropic media (for nonisotropic media, one would need to replace the assumed scalar susceptibilities with tensors). We note that there are many situations in ultrafast optics where these assumptions are not valid. For example, nonlinear optical effects, which we discuss in later chapters, require by definition that $\mathbf{P}$ be a nonlinear function of $\mathbf{E}$.

1.2.2 The Wave Equation and Plane Waves

We now consider electromagnetic wave propagation in linear, isotropic, source-free media. To derive the wave equation, we take the curl of eq. (1.3) and insert eq. (1.4), which, using the stated assumptions and a well-known vector identity,[1] gives the following:

$$\nabla \times \nabla \times \mathbf{E} = \nabla\,(\nabla \cdot \mathbf{E}) - \nabla^2\mathbf{E} = -\mu\varepsilon\frac{\partial^2\mathbf{E}}{\partial t^2} \tag{1.14}$$

[1] The identity is $\nabla \times \nabla \times \mathbf{A} = \nabla(\nabla \cdot \mathbf{A}) - \nabla^2\mathbf{A}$. Note that in Cartesian coordinates ∇^2 has a very simple form, namely $\nabla^2\mathbf{A} = (\partial^2/\partial x^2 + \partial^2/\partial y^2 + \partial^2/\partial z^2)\mathbf{A}$.

Since $\nabla \cdot \mathbf{E} = 0$ also under our conditions, we obtain the wave equation

$$\nabla^2 \mathbf{E} = \mu\varepsilon \frac{\partial^2 \mathbf{E}}{\partial t^2} \tag{1.15}$$

One situation of special interest is the case where the field varies in only one direction, which without loss of generality we take as the z direction. Then the wave equation becomes

$$\frac{\partial^2 \mathbf{E}}{\partial z^2} = \mu\varepsilon \frac{\partial^2 \mathbf{E}}{\partial t^2} \tag{1.16}$$

The general solution takes the form

$$\mathbf{E}(z, t) = \mathbf{E}_0 \left(t - \frac{z}{v} \right) \tag{1.17}$$

where $\mathbf{E}_0$ is a vector in the x–y plane [eq. (1.1) precludes E from having a z-component] and $v = 1/\sqrt{\mu\varepsilon}$. The solution can be verified by plugging back into the wave equation. Equation (1.17) is called a *plane-wave solution*, since the field does not vary in the transverse (x–y) plane. It also represents a traveling wave, since the field propagates in the z direction without changing its form. In the case of a pulsed field, $\mathbf{E}_0(t)$ represents the pulse shape. The propagation velocity is given by v. Note that

$$\frac{1}{\sqrt{\mu_0 \varepsilon_0}} = c \cong 2.998 \times 10^8 \, \mathrm{m\,s^{-1}} \tag{1.18}$$

is the velocity of light in free space. Therefore, for the case most common in optics where $\mu = \mu_0$, the velocity of propagation within a medium is given by

$$v = \frac{c}{n} \tag{1.19}$$

where n is the refractive index according to eq. (1.10). Note also that in deriving eqs. (1.14) to (1.17), we have assumed implicitly that the refractive index n is independent of frequency. When n does have a frequency dependence, this can change the propagation velocity or cause the pulse to distort during propagation. These effects are discussed in Chapter 4.

The case of a sinusoidal solution to the wave equation will be of special importance. Then eq. (1.17) takes the form

$$\mathbf{E}(z, t) = \mathbf{E}_0 \cos(\omega t - kz + \phi) \tag{1.20}$$

where $\mathbf{E}_0$ is now a constant vector, ω is the angular frequency, and the propagation constant k must satisfy the dispersion relation

$$k = \omega\sqrt{\mu\varepsilon} \tag{1.21}$$

or again, assuming that $\mu = \mu_0$,

$$k = \frac{\omega n}{c} \tag{1.22}$$

The wave has a temporal oscillation period equal to $2\pi/\omega$ and a spatial period or wavelength *in the medium* given by $\lambda = 2\pi/k$. The wavelength in free space is denoted λ_0 and is given by

$$\lambda_0 = \frac{2\pi c}{\omega} \tag{1.23}$$

Equation (1.20) represents the ideal case of single frequency or monochromatic laser radiation. It can also be written in the equivalent form

$$\mathbf{E}(z, t) = \mathrm{Re}\left\{\tilde{\mathbf{E}}_0 e^{j(\omega t - kz)}\right\} \tag{1.24}$$

where $\mathrm{Re}\{\cdots\}$ denotes the real part and the phase ϕ has been incorporated into the complex vector $\tilde{\mathbf{E}}_0$. We refer to this form as complex notation. As we will see shortly, ultrashort light pulses are conveniently described as superpositions of sinusoidal solutions of the form (1.20) or (1.24) with different frequencies.

Finally, we note that similar solutions can be written for propagation in directions other than along z, as follows:

$$\mathbf{E}(\mathbf{r}, t) = \mathrm{Re}\left\{\tilde{\mathbf{E}}_0 e^{j(\omega t - \mathbf{k}\cdot\mathbf{r})}\right\} \tag{1.25}$$

Here $\mathbf{k}$ is the propagation vector; it points along the direction of propagation and its magnitude $k = |\mathbf{k}|$ still satisfies the dispersion relation (1.21).

1.2.3 Poynting's Vector and Power Flow

We also review the expressions for energy flow with electromagnetic waves. To arrive at the required formulas, we form the dot product of eq. (1.3) with $\mathbf{H}$ and subtract from this the dot product of eq. (1.4) with $\mathbf{E}$. Using another vector identity,[2] we find that

$$\nabla \cdot (\mathbf{E} \times \mathbf{H}) + \mathbf{H} \cdot \frac{\partial \mathbf{B}}{\partial t} + \mathbf{E} \cdot \frac{\partial \mathbf{D}}{\partial t} + \mathbf{E} \cdot \mathbf{J} = 0 \tag{1.26}$$

We also make use of the divergence theorem,

$$\int \nabla \cdot \mathbf{A}\, dV = \int \mathbf{A} \cdot \hat{\mathbf{n}}\, dS \tag{1.27}$$

which states that the surface integral of a vector $\mathbf{A}$ over a closed surface is equal to the volume integral of $\nabla \cdot \mathbf{A}$ over the volume bounded by that surface. $\hat{\mathbf{n}}$ is the unit vector

[2] The identity is $\nabla \cdot \mathbf{A} \times \mathbf{B} = \mathbf{B} \cdot \nabla \times \mathbf{A} - \mathbf{A} \cdot \nabla \times \mathbf{B}$.

normal to the surface and pointing outward. The result is

$$\int (\mathbf{E} \times \mathbf{H}) \cdot \hat{\mathbf{n}}\, dS + \int dV \left\{ \mathbf{H} \cdot \frac{\partial \mathbf{B}}{\partial t} + \mathbf{E} \cdot \frac{\partial \mathbf{D}}{\partial t} + \mathbf{E} \cdot \mathbf{J} \right\} = 0 \tag{1.28}$$

Finally, assuming a linear medium and substituting for $\mathbf{D}$ and $\mathbf{B}$ using eqs. (1.8) and (1.12), we obtain

$$\int (\mathbf{E} \times \mathbf{H}) \cdot \hat{\mathbf{n}}\, dS + \int dV \left\{ \frac{\partial \left(\frac{1}{2} \varepsilon |\mathbf{E}|^2 \right)}{\partial t} + \frac{\partial \left(\frac{1}{2} \mu |\mathbf{H}|^2 \right)}{\partial t} + \mathbf{E} \cdot \mathbf{J} \right\} = 0 \tag{1.29}$$

Equations (1.28) and (1.29) are representations of Poynting's theorem, which describes conservation of energy in electromagnetic systems. We can identify specific meanings for each of the terms. Look at eq. (1.29), for example:

- $\int (\mathbf{E} \times \mathbf{H}) \cdot \hat{\mathbf{n}}\, dS$ is the net rate of energy flow out of the closed surface. It has units of power (watts). $\mathbf{E} \times \mathbf{H}$ is called the *Poynting vector* and has units of intensity (W/m^2). It gives the power density carried by an electromagnetic wave and the direction in which power is carried.
- $\frac{1}{2} \varepsilon |\mathbf{E}|^2$ and $\frac{1}{2} \mu |\mathbf{H}|^2$ are the local energy densities (J/m^3) associated with the electric and magnetic fields, respectively. $\partial / \partial t \int \frac{1}{2} \varepsilon |\mathbf{E}|^2\, dV$ and $\partial / \partial t \int \frac{1}{2} \mu |\mathbf{H}|^2\, dV$ represent the time rate of change of electric and magnetic field energy stored within the volume, respectively.
- $\int \mathbf{E} \cdot \mathbf{J}\, dV$ represents power dissipation or generation within the volume (in watts). When $\mathbf{E} \cdot \mathbf{J}$ is positive, this term represents power dissipation due, for example, to ohmic losses. Energy is transferred out of the fields and into the medium, typically as heat. When $\mathbf{E} \cdot \mathbf{J}$ is negative, this term represents power supplied by the currents and fed into the electromagnetic fields.

Overall, Poynting's theorem is a power balance equation, showing how changes in stored energy are accounted for by power dissipation and energy flow.

It is worth specializing once more to the case of single-frequency sinusoidal fields, with $\mathbf{E}$ given by eq. (1.25). The $\mathbf{H}$ field is obtained using eq. (1.3), with the result

$$\mathbf{H} = \mathrm{Re} \left\{ \sqrt{\frac{\varepsilon}{\mu}} \frac{\mathbf{k} \times \tilde{\mathbf{E}}_0}{k} e^{j(\omega t - \mathbf{k} \cdot \mathbf{r})} \right\} \tag{1.30}$$

Thus $\mathbf{H}$ is perpendicular to both $\mathbf{E}$ and $\mathbf{k}$, and its magnitude is equal to $\sqrt{\varepsilon / \mu}\, |\mathbf{E}|$. The factor $\sqrt{\mu / \varepsilon}$ is termed the *characteristic impedance* of the medium, and $\sqrt{\varepsilon / \mu}$ is therefore the *admittance*.

In optics one is usually interested in the time-average power flow. This is calculated in complex notation as follows. First consider scalar functions $f(t)$ and $g(t)$, where

$$f(t) = \mathrm{Re}\left\{\tilde{f}e^{j\omega t}\right\} \qquad \text{and} \qquad g(t) = \mathrm{Re}\left\{\tilde{g}e^{j\omega t}\right\} \tag{1.31}$$

The time average of $f(t)g(t)$ is given by

$$\langle fg\rangle = \frac{1}{2}\mathrm{Re}\left\{\tilde{f}\tilde{g}^*\right\} \tag{1.32}$$

Here $\langle\cdots\rangle$ denotes the time average and * indicates a complex conjugate. Similarly, if $\mathbf{f}(t)$, $\mathbf{g}(t)$, $\tilde{\mathbf{f}}$, and $\tilde{\mathbf{g}}$ now denote vectors, the time average of $\mathbf{f}\times\mathbf{g}$ is given by

$$\langle \mathbf{f}\times\mathbf{g}\rangle = \frac{1}{2}\mathrm{Re}\left\{\tilde{\mathbf{f}}\times\tilde{\mathbf{g}}^*\right\} \tag{1.33}$$

Using these relations, the time-average Poynting vector for the plane waves of eqs. (1.25) and (1.30) becomes

$$\langle \mathbf{E}\times\mathbf{H}\rangle = \frac{1}{2}\sqrt{\frac{\varepsilon}{\mu}}\left|\tilde{\mathbf{E}}_0\right|^2\frac{\mathbf{k}}{k} \tag{1.34}$$

where we have assumed that ε and μ are real. Power is carried along the direction of $\mathbf{k}$. In the case of a nonmagnetic material, we can write the magnitude of the time-average Poynting vector, commonly called the *intensity* I, in the following useful form:

$$I = \left|\langle \mathbf{E}\times\mathbf{H}\rangle\right| = \frac{1}{2}\varepsilon_0 cn\left|\tilde{\mathbf{E}}_0\right|^2 \tag{1.35}$$

1.3 REVIEW OF LASER ESSENTIALS

We will shortly discuss in some detail methods by which lasers can be made to produce ultrashort light pulses. First, however, we give a brief and simple review of lasers in general. More detail can be found in texts on lasers, such as [7,8].

1.3.1 Steady-State Laser Operation

Schematic drawings of two simple laser geometries are shown in Fig. 1.1. Both lasers consist of a set of mirrors and a gain medium. The gain medium is an optical amplifier which coherently amplifies light passing through it. The mirrors may be curved or planar and together make up the laser cavity or resonator. The cavity is aligned so that light reflects back and forth again and again, passing along the same path every time. If we imagine even a very weak light intensity in the cavity (due to spontaneous emission from the gain medium), then for sufficiently high gain, the intensity increases from one round trip through the laser to the next, eventually resulting in an intense beam. In steady state the gain per round trip must equal the loss. Part of the light passes through the partially transmissive output coupler, and this forms the output laser beam, which can be used for experiments.

cross-correlation measurements described in Section 3.3.1. With full fringe data one may extract new information through Fourier transform analysis. For example, in Doppler OCT one assigns shifts in interferogram spectra to shifts in the mean frequency of back-scattered light [107,108]. Such frequency shifts provide information on scatterer velocities, projected in the direction of light propagation, through the Doppler effect. Furthermore, by analyzing Doppler OCT data in terms of joint time–frequency distributions (see Section 3.5), it becomes possible to acquire depth-resolved velocity images. This approach has enabled mapping of flow in subsurface blood vessels in living tissues.

3.4 INTENSITY CORRELATION MEASUREMENTS

3.4.1 Correlation Measurements Using Second-Harmonic Generation

We have already seen that in the case of a single unknown pulse, a common measurement strategy is to arrange for the pulse to sample itself. Mathematically, this means that one measures a correlation function of the pulse. We have also seen that measurement of the electric field autocorrelation function using a linear Michelson interferometer does not provide any new information about the pulse. To perform a more useful measurement, one can insert a nonlinear element into the interferometer. The most common approach involves second-harmonic generation (SHG), in which a nonlinear crystal is used to generate light at twice the input optical frequency (i.e., at the second harmonic $2\omega_0$ of the input light at the fundamental frequency ω_0). The measurement procedure is to record the time-averaged second-harmonic power as a function of the relative delay τ between the two identical versions of the input pulse [109–112]. Due to the nonlinearity, the total energy in the second-harmonic pulse is greater when the two pulses incident on the nonlinear crystal overlap in time. Therefore, the peak in second-harmonic power plotted as a function of τ contains information about the pulse width. For an excellent discussion of SHG and other nonlinear correlation techniques, see [113].

We now analyze this SHG measurement in the collinear geometry shown in Fig. 3.8. We assume (1) that the intensity is low enough to avoid saturation associated with pump

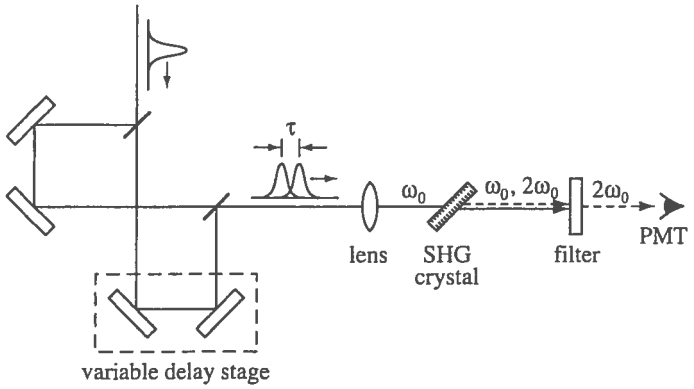

Figure 3.8 Collinear second-harmonic generation geometry for measurement of the intensity autocorrelation function. PMT, photomultiplier tube.

depletion and (2) that the bandwidth of the SHG process is large enough to accommodate the entire spectrum. The first assumption is easily met in practice. The second criterion requires the use of thin nonlinear crystals, especially for very short pulses, so that second-harmonic generation is *phase matched* over a sufficiently broad spectrum. The concept of phase matching and its implications for the bandwidth of the SHG process are discussed in Chapter 5.

The field emerging out of the interferometer and incident on the SHG crystal is written

$$e_{\text{out}}(t) = \frac{1}{2}\text{Re}\{a(t)e^{j\omega_0 t} + a(t-\tau)e^{j\omega_0(t-\tau)}\} \tag{3.34}$$

The field at the second-harmonic frequency, which is proportional to the square of input field, is given by

$$\begin{aligned} e_{\text{SHG}}(t) &\sim e_{\text{out}}^2(t) \\ &\sim \text{Re}\{[a^2(t) + a^2(t-\tau)e^{-2j\omega_0\tau} + 2a(t)a(t-\tau)e^{-j\omega_0\tau}]e^{2j\omega_0 t}\} \end{aligned} \tag{3.35}$$

The actual measurement records the time-integrated (or equivalently, the time-averaged) second-harmonic power (not the instantaneous power, since this would require an ultrafast detector, which we have assumed is not available). After some algebra one obtains the following expression:

$$\begin{aligned} \langle P_{\text{SHG}}(t)\rangle \sim{}& 2\langle|a(t)|^4\rangle + 4\langle|a(t)|^2|a(t-\tau)|^2\rangle + \{\{2\langle(|a(t)|^2 + |a(t-\tau)|^2) \\ &\times a(t)a^*(t-\tau)\rangle e^{j\omega_0\tau} + \langle[a(t)a^*(t-\tau)]^2\rangle e^{2j\omega_0\tau}\} + \text{c.c.}\} \end{aligned} \tag{3.36}$$

In arriving at this expression, we have assumed a time-stationary process, as previously. The first term in eq. (3.36) is independent of τ, and the second term varies relatively slowly with τ. The third and fourth terms represent interferometric contributions at frequencies ω_0 and $2\omega_0$, respectively, which oscillate rapidly as τ is varied over one optical period.

Fringe-Averaged Autocorrelation Often, one suppresses the interferometric terms by averaging the SHG signal over a few optical periods. The measured time-average second-harmonic power then becomes

$$\langle P_{\text{SHG}}(t)\rangle \sim \langle|a(t)|^4\rangle\left(1 + \frac{2\langle|a(t)|^2|a(t-\tau)|^2\rangle}{\langle|a(t)|^4\rangle}\right) \tag{3.37}$$

At this point we define the normalized intensity autocorrelation function $G_2(\tau)$:

$$G_2(\tau) = \frac{\langle I(t)I(t-\tau)\rangle}{\langle|I(t)|^2\rangle} \tag{3.38}$$

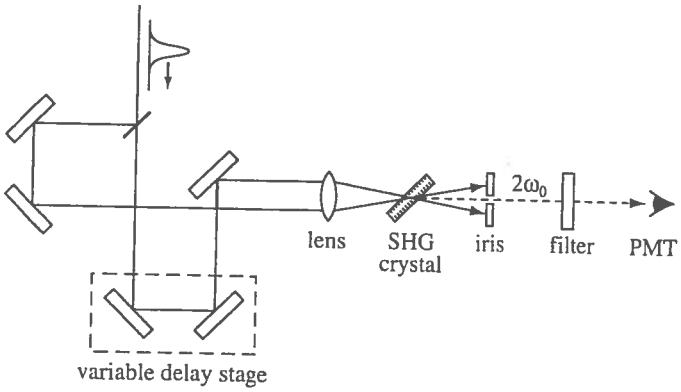

Figure 3.9 Noncollinear second-harmonic generation geometry for background-free intensity autocorrelation function measurement. PMT, photomultiplier tube.

where $I(t) \sim |a(t)|^2$ as usual. Equation (3.37) for the time-average second harmonic power in a collinear measurement geometry then becomes

$$\langle P_{\mathrm{SHG}}(t) \rangle \sim 1 + 2G_2(\tau) \tag{3.39}$$

The measured second-harmonic power is the sum of a constant background term (which represents the SHG from each pulse individually) and twice the intensity autocorrelation function (which arises from the interaction of the two time-delayed pulses).

Another common experimental arrangement uses a noncollinear geometry (Fig. 3.9), in which the second harmonic due to the interaction between the time-delayed pulses is emitted in a different direction than that due to the individual pulses. In this case, the constant background terms can be suppressed, both by using an iris and by adjusting the SHG phase-matching conditions. The output signal in the background-free noncollinear geometry becomes

$$\langle P_{\mathrm{SHG}}(t) \rangle \sim G_2(\tau) \tag{3.40}$$

Note that the noncollinear geometry automatically averages out the fringe terms in eq. (3.36).

It is useful at this point to comment on the properties of $G_2(\tau)$. Several important points are listed below.

- The normalized intensity correlation function assumes its maximum value of unity at $\tau = 0$.
- In the case of finite-duration pulses, the pulses exhibit no overlap for delays much greater than the pulse width, and the correlation function goes to zero. The width of the correlation peak gives information about the pulse width.
- The correlation function is an even function of τ, independent of the symmetry of the actual pulse. Therefore, one cannot uniquely recover the pulse intensity profile from $G_2(\tau)$.

- If one somehow knew a priori that the intensity profile were symmetric, one could indeed recover $I(t)$ from $G_2(\tau)$. We note that the Fourier transform of $G_2(\tau)$ is $\left|\tilde{I}(\omega)\right|^2$, where $\tilde{I}(\omega)$ is the Fourier transform of $I(t)$. If $I(t)$ is symmetric, $\tilde{I}(\omega)$ must be real; therefore, $\tilde{I}(\omega)$ can be obtained by taking the square root of $\left|\tilde{I}(\omega)\right|^2$.
- Conversely, in the usual case where $I(t)$ is not known to be symmetric, $\tilde{I}(\omega)$ cannot be assumed real. Therefore, $G_2(\tau)$ only gives $\left|\tilde{I}(\omega)\right|$ and not its phase, which would be needed to reconstruct $I(t)$.
- By definition, the intensity autocorrelation function is also insensitive to the phase of the electric field itself. Therefore, the fringe-averaged intensity autocorrelation $G_2(\tau)$ cannot be used to characterize chirps or phase modulations on the pulse.

It is also worth discussing the behavior of $G_2(\tau)$ in the case of continuous-wave noise [113]. The intensity correlation function still takes on its maximum value of unity at $\tau = 0$. However, for sufficiently large values of τ, the two relatively delayed versions of the same noise signal are uncorrelated. Since the intensity is always nonnegative, the correlation never drops to zero, but the value is reduced below unity. This results in a coherence peak in the intensity autocorrelation function. It is important to note that this coherence peak has nothing to do with the actual pulse width; the width of the peak is governed by the correlation time of the intensity fluctuations, which can be as short as the inverse of the optical bandwidth. For the specific common case of a Gaussian random field (i.e., the real and imaginary parts of the electric field are independent, zero-mean random variables described by Gaussian probability distributions with equal variances), the probability distribution $p_I(I)$ for the intensity is given by

$$p_I(I) = \frac{1}{\langle I \rangle} e^{-I/\langle I \rangle} \tag{3.41}$$

where $\langle I \rangle$ is the average intensity. At delays large enough so that the two noise signals are independent, we get

$$G_2(\tau) = \frac{\langle I(t) \rangle^2}{\langle I^2(t) \rangle} = \frac{1}{2} \tag{3.42}$$

where we have used $\langle f(I) \rangle = \int dI\, f(I) p_I(I)$.

These findings are summarized in Fig. 3.10. In the collinear measurement geometry, the correlation function for a single coherent pulse decays smoothly to a constant background level, with a 3 : 1 contrast ratio between the peak at $\tau = 0$ and the background. This theoretical contrast ratio can be used as a check for proper experimental alignment. In the case of continuous-wave noise, the only feature is the coherence spike centered near $\tau = 0$, with a contrast ratio of 3 : 2. The intermediate case of a finite-duration noise burst has a coherence spike centered on top of a finite-duration pedestal, with a contrast ratio of 3 : 2 : 1. It is important not to use the duration of the coherence spike to estimate the pulse duration, and it also important to note that the intensity autocorrelation of a pulse with a smooth intensity profile but containing excess bandwidth in the form of a chirp will not exhibit a coherence spike, which arises only from substructure in the intensity. One can estimate the pulse duration from the full width at half maximum (FWHM) of the correlation trace (excluding coherence spike), denoted $\Delta\tau$ in the figure.

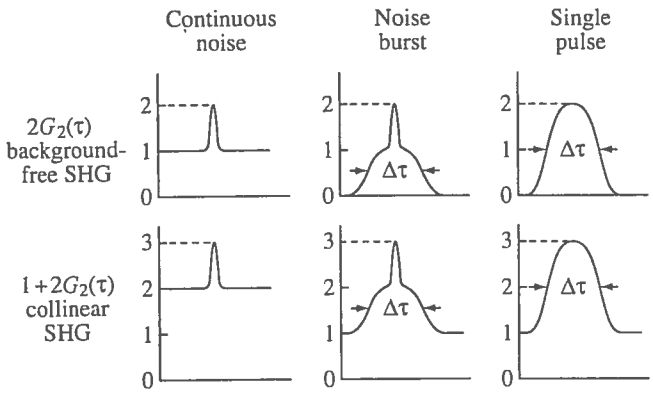

Figure 3.10 Theoretical traces for collinear and noncollinear SHG autocorrelation measurements. From Fig. 3.3 of [113], with permission from Springer Science and Business Media.

The situation is similar in the noncollinear measurement geometry, except that there is no constant background for finite-duration pulses. The zero background makes it easier to identify small amounts of energy in the wings of the pulse. The contrast ratio is 2 : 1 for continuous-wave noise and 2 : 1 : 0 for a finite-duration noise burst.

To estimate the intensity FWHM pulse width from the autocorrelation, one must assume a specific pulse shape. The intensity FWHM (Δt) is then determined by dividing the intensity autocorrelation FWHM ($\Delta\tau$) by a pulse-shape-specific deconvolution factor. See Table 3.2 for autocorrelation functions and deconvolution factors for a few different pulse shapes [113,114]. For smoothly varying pulse shapes (e.g., Gaussian or sech^2 pulses), the variation in the deconvolution factor is of order 10%, and therefore the pulse duration can be obtained approximately, even though the pulse shape is not, in fact, known. For less-well-behaved pulses (e.g., rectangular or single-sided exponential pulses), the deconvolution factor can vary by a larger amount. To do a consistency check, one can fit the autocorrelation data to the functional form of $G_2(\tau)$ corresponding to the assumed pulse shape. It is also useful to compare the measured time–bandwidth product $\Delta\nu\,\Delta t$ with that corresponding to the assumed pulse shape. A discrepancy between the experimental and theoretical time–bandwidth product indicates either a deviation from the assumed pulse shape or the presence of chirp. Note, however, that these consistency checks do not

Table 3.2 Autocorrelation Functions and Deconvolution Factors for Four Pulse Shapes[a]

$I(t)$	$G_2(\tau)$	$\frac{\Delta\tau}{\Delta t}$
$\text{sq}(t)$	$1 - \lvert\tau\rvert$ for $\lvert\tau\rvert \le 1$, 0 otherwise	1
e^{-2t^2}	$e^{-\tau^2}$	$\sqrt{2}$
$\text{sech}^2(t)$	$\dfrac{3(\tau\cosh(\tau) - \sinh(\tau))}{\sinh^3(\tau)}$	1.543
e^{-t} for $t \ge 0$, 0 otherwise	$e^{-\lvert\tau\rvert}$	2

[a] Δt and $\Delta\tau$ are full widths at half maximum of the intensity $I(t)$ and the intensity autocorrelation function $G_2(\tau)$, respectively. $\text{sq}(u)$ is defined as a unit square pulse such that $\text{sq}(u) = 1$ for $\lvert u\rvert \le \frac{1}{2}$ and 0 otherwise; and t and τ are in normalized units.

assure uniqueness (i.e., it is still possible that the actual pulse shape deviates from the shape assumed).

Additional information is available using the root-mean-square (rms) pulse width Δt_{rms}, as discussed in [94]. The definition of the rms pulse width was given in Section 3.1. A very useful property of the rms pulse width is that it can be found directly from the intensity autocorrelation function without any assumption about the pulse shape using the following formula:

$$(\Delta t_{\text{rms}})^2 = \frac{2\int d\tau\, \tau^2 G_2(\tau)}{\int d\tau\, G_2(\tau)} \tag{3.43}$$

It was also demonstrated that for a given power spectrum $|E(\omega)|^2$, Δt_{rms} assumes its minimum value $\Delta t_{\text{rms}}^{(0)}$ when $E(\omega)$ has a constant spectral phase [i.e., when $E(\omega)$ is bandwidth-limited]. A similar relation is often assumed for the FWHM pulse width Δt, but there is no proof of this assumption. Based on this minimum rms pulse width theorem, Sorokin et al. [94] also introduced an rms chirp parameter

$$C = \sqrt{\langle \tau^2(\omega) \rangle - \langle \tau(\omega) \rangle^2} \tag{3.44}$$

which they showed could also be expressed in terms of the rms pulse widths:

$$C = \frac{1}{2}\sqrt{(\Delta t_{\text{rms}})^2 - \left(\Delta t_{\text{rms}}^{(0)}\right)^2} \tag{3.45}$$

In these expressions $\tau(\omega)$ is the frequency-dependent delay as defined in eq. (2.82), and eq. (3.8) is used. An increase in Δt_{rms} over the bandwidth-limited value $\Delta t_{\text{rms}}^{(0)}$ gives a direct indication of spectral chirp, as quantified through the C parameter. An attractive feature of this definition is that both Δt_{rms} and $\Delta t_{\text{rms}}^{(0)}$ can be obtained directly from commonly available experimental diagnostics: Δt_{rms} from intensity autocorrelation through eq. (3.43) and $\Delta t_{\text{rms}}^{(0)}$ by taking the square root of the power spectrum, assuming constant phase, and Fourier transforming to get $I(t)$.

Interferometric Autocorrelation We now return to the full expression describing the SHG pulse-width measurement including interferometric terms, eq. (3.36). Detailed information on interpreting interferometric autocorrelation data is given in [95,114]. The interferometric terms include some phase and coherence information that is lacking in $G_2(\tau)$ itself. These terms may be recorded by using a collinear measurement geometry and exercising care to avoid averaging over the rapid interferometric oscillations. As an example, consider the data plotted in Figs. 3.11 and 3.12, which correspond to pulses from a self-mode-locked Ti:S. Figure 3.11 corresponds to pulses obtained when a prism pair is used for intracavity dispersion compensation. The intensity autocorrelation function is smooth and yields a 60-fs intensity FWHM pulse duration assuming a sech^2 intensity profile. The width of the power spectrum is such that the time–bandwidth product is $\Delta\nu\, \Delta t \approx 0.33$, in close agreement with the theoretical value of 0.315 for secant hyperbolic pulses. Thus, these pulses appear to be close to *bandwidth limited*, meaning that (1) the pulse duration is as short as it can be given the mode-locked bandwidth, and (2) there is little or no chirp. The most notable

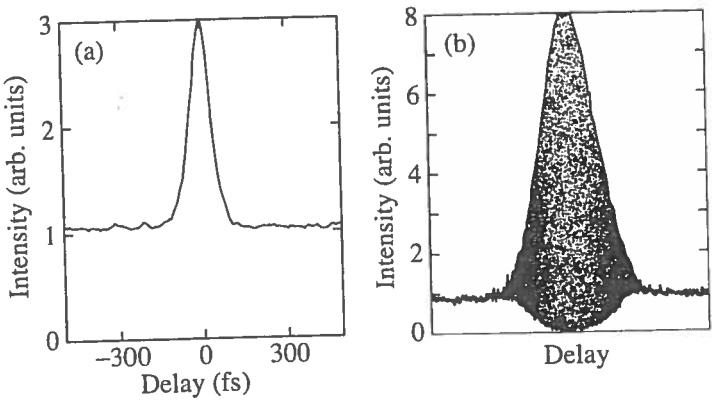

Figure 3.11 (a) Intensity autocorrelation and (b) interferometric autocorrelation for nearly bandwidth-limited pulses from a mode-locked Ti:S laser. A 60-fs pulse width and a time–bandwidth product $\Delta\nu\,\Delta t = 0.33$ are calculated assuming a sech^2 intensity profile. For (b), the delay axis is zoomed by roughly a factor of 3 compared to (a). From [52].

feature of the interferometric autocorrelation is that the fringes last throughout the entire pulse duration. This is another sign that the pulse is bandwidth limited.

The situation is rather different in Fig. 3.12, which corresponds to data obtained when the prism pair is removed from the laser. In this case the dispersion in the laser cavity is dominated by the Ti:S crystal and is large and positive. Comparing with Figs. 2.19 and 2.20, one expects relatively long mode-locked pulses with a strong chirp. This expectation is confirmed by the measurements. The intensity autocorrelation remains smooth (no coherence spike), but with the intensity FWHM pulse duration broadened to 2 ps (again assuming sech^2 pulses). At the same time the spectral width is narrowed from 14 nm to 3.5 nm. The calculated time–bandwidth product increases to 2.7, indicating that the pulses are far from the bandwidth limit. The appearance of the interferometric autocorrelation is changed dramatically: The fringes now occur only near the center of the trace and die off

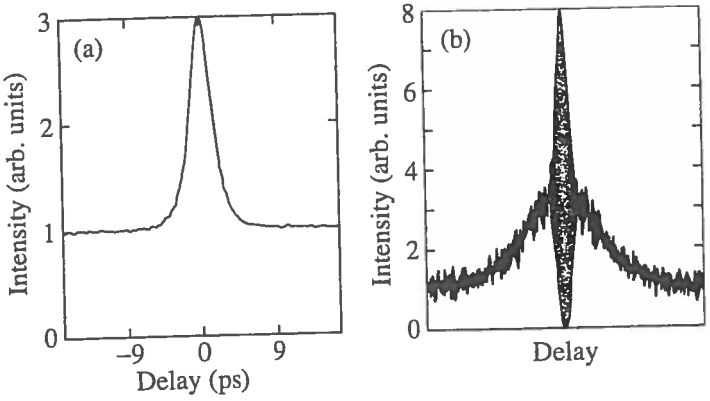

Figure 3.12 (a) Intensity autocorrelation and (b) interferometric autocorrelation for highly chirped pulses from a mode-locked Ti:S laser. A 2-ps pulse width and a time–bandwidth product $\Delta\nu\,\Delta t = 2.7$ are calculated assuming a sech^2 intensity profile. For (b), the delay axis is zoomed by roughly a factor of 3 compared to (a). From [52].

much faster than the nonoscillating portion of the experimental trace. The envelope of the fringes is related to the inverse of the spectral bandwidth (but in a more complicated way than in electric field autocorrelation). The data indicate that the coherence time of the pulses is much shorter than the duration of the intensity profile, consistent with the large $\Delta\nu\ \Delta t$ product and a strong chirp. This behavior should not be confused with coherence spikes which can be observed in measurements of $G_2(\tau)$, which arise due to noise substructure on the intensity profile and are insensitive to chirp.

It is also worth discussing the contrast ratio observed in interferometric autocorrelation measurements. The upper envelope of the fringes results when the two time-delayed fields are exactly in phase and add to produce a maximum total field; the lower envelope results when the two fields are exactly out of phase and cancel to produce the minimum total field. For the case where the coherence time is essentially equal to the pulse width (i.e., the temporal phase is essentially constant), the upper and lower envelopes are proportional to

$$\text{upper envelope} \sim \left\langle\ [|a(t)| + |a(t-\tau)|]^4\ \right\rangle \tag{3.46a}$$

$$\text{lower envelope} \sim \left\langle\ [|a(t)| - |a(t-\tau)|]^4\ \right\rangle \tag{3.46b}$$

where the two pulses are also assumed to have equal amplitudes. When there is significant phase modulation (i.e., the coherence time is shorter than the pulse width), this equation applies only for $|\tau| \ll \tau_c$; for $|\tau| \gg \tau_c$ the fringes disappear and only the nonoscillating terms given by eq. (3.39) remain. In all cases the background level observed for large delays when the pulses no longer overlap is proportional to

$$\text{background} \sim 2\left\langle |a(t)|^4 \right\rangle \tag{3.47}$$

From these formulas we can easily see that the contrast ratio between the peak of the upper fringe envelope and the background level should be 8 : 1, as observed in the data shown above. The lower envelope is at the zero level near $\tau = 0$, also as observed. If one averages over the fringes, one gets back to $1 + 2G_2(\tau)$ as indicated in eq. (3.39), with a contrast ratio of 3 : 1 between the peak and the background. (This last statement is not obvious from Figs. 3.11 and 3.12 but is true nevertheless!)

Note that the presence or absence of strong chirp in Figs. 3.11 and 3.12 could be deduced from the time–bandwidth product alone, without using the interferometric autocorrelation. The interferometric autocorrelation is useful because it can serve as a clear visual indicator of moderate to large chirp and because it provides additional data for quantitative pulse-shape analysis. It has been shown that if one measures the term varying as $\exp\{2j\omega_0\tau\}$ in the interferometric autocorrelation, that is,

$$\Xi(\tau) = \left\langle \left[a(t)a^*(t-\tau)\right]^2 \right\rangle e^{2j\omega_0\tau}$$

then together with the fringe-averaged autocorrelation $G_2(\tau)$ and the power spectrum of the input pulse $|A(\omega - \omega_0)|^2$, this is enough information to determine the complete electric field profile uniquely[3] [115]. Reconstruction of the electric field from these data has been

[3] The electric field is determined uniquely except for a time-reversal ambiguity; $a(t)$ and $a^*(-t)$ are both allowed solutions. Furthermore, the proof assumes that the field has finite support (i.e., it is strictly zero outside a finite time window).

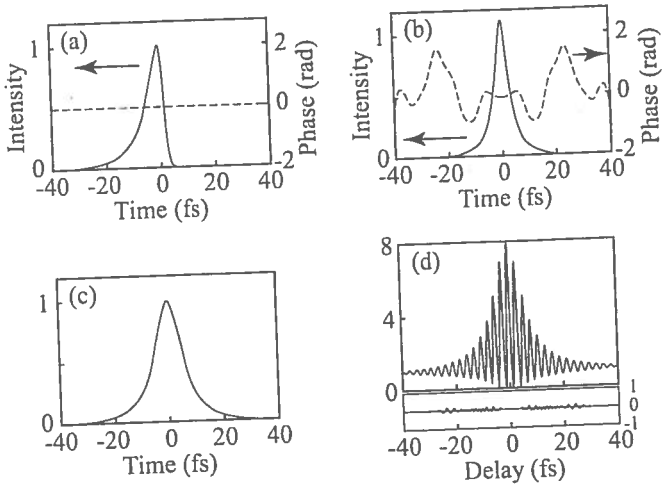

Figure 3.13 Calculation results for a pair of pulses constructed to have identical fringe-averaged autocorrelation traces and power spectra: (a) asymmetric pulse; (b) symmetric pulse; (c) fringe-averaged autocorrelation trace, identical for both pulses; (d) interferometric autocorrelation of asymmetric pulse (top) and difference in asymmetric and symmetric pulse interferometric autocorrelations (bottom). Adapted from [116]. Copyright ©2001, IEEE.

demonstrated by using iterative phase retrieval techniques related to those described later in Section 3.6.5. Practically, this technique has seen limited use, possibly because of the need for high measurement accuracy to ensure valid reconstruction of $a(t)$. It is also interesting that in the case of a pulse free of frequency modulation, the term multiplying $\exp\{2j\omega_0\tau\}$ in $\Xi(\tau)$ is identical to $G_2(\tau)$. Therefore, by carefully comparing these two terms, one can directly check whether $a(t)$ is real. Finally, we note that $\Xi(\tau)$ is simply the electric field autocorrelation of the second-harmonic pulse $a^2(t)$ produced in response to a single pulse illuminating the second-harmonic crystal. Therefore, measurement of the power spectrum of a single second-harmonic pulse gives equivalent information.

These points are illustrated in Fig. 3.13, which shows calculation results for a pair of pulses constructed to have identical fringe-averaged autocorrelation traces and power spectra. One of the pulses (Fig. 3.13a) has an asymmetric intensity profile with a 28-fs FHWM pulse width and a flat temporal phase, while the other (Fig. 3.13b) has a symmetric intensity profile with a 37-fs FWHM pulse width and phase modulation. $G_2(\tau)$ is shown in Fig. 3.13c and is identical for both pulses, as stated. This demonstrates the ambiguity inherent in fringe-averaged intensity autocorrelation measurements. Figure 3.13d shows the interferometric autocorrelation of the asymmetric pulse. The interferometric autocorrelation of the symmetric pulse is almost identical and is not included in the main frame of Fig. 3.13d. Instead, the difference between the two interferometric autocorrelations is plotted in the lower part of Fig. 3.13d. The rms difference between the two traces is less than 1%. Thus, although the interferometric autocorrelations of the two pulses are in fact distinct, as predicted [115], the differences are subtle. The conclusion is that interferometric autocorrelation data may be only weakly sensitive to rather significant changes in pulse shape and may therefore be quite challenging to apply for unambiguous pulse-shape retrieval in a practical experimental context.

9

ULTRAFAST TIME-RESOLVED SPECTROSCOPY

9.1 INTRODUCTION TO ULTRAFAST SPECTROSCOPY

A major application of femtosecond pulses is for time-resolved studies of ultrafast dynamical processes in chemical, solid-state, and biological materials. Just as high-speed (microsecond) electronic flashes have been used for many decades to make stop-action photographs of rapid (microseconds and slower) mechanical motions of macroscopic objects [2], ultrashort laser pulses are a unique tool for excitation and stop-action measurements of ultrafast microscopic and quantum mechanical processes within materials. Examples include scattering of photoexcited charge carriers in a solid-state crystal lattice, dynamics of solvated chemical species interacting with their fluctuating liquid-state environment, oscillatory wave packet motions arising due to the interference between coherently excited quantum mechanical eigenstates, and many more. Detailed treatments of time-resolved spectroscopy of ultrafast physical processes in chemical and semiconductor systems may be found in [505,506] and [249], respectively.

A large number of different ultrafast spectroscopy schemes may be understood within the framework of the pump–probe approach (e.g., [113]), illustrated in Fig. 9.1. A short pump pulse first impinges upon the sample under investigation and excites it in some way. This excitation induces a change in some material property $\mathcal{P}$, which in most cases of interest to us is an optical property. We may write

$$\mathcal{P}(t) \rightarrow \mathcal{P}_0 + \Delta\mathcal{P}(t - t_0) \tag{9.1}$$

where $\mathcal{P}_0$ and $\Delta\mathcal{P}$ are the initial value of property $\mathcal{P}$ and the change in $\mathcal{P}$ induced by a pump pulse arriving at time t_0, respectively. A second pulse, termed the *probe*, arrives at the sample with time delay τ relative to the pump pulse. Often, the intensity of the probe

Ultrafast Optics, By Andrew M. Weiner
Copyright © 2009 John Wiley & Sons, Inc.

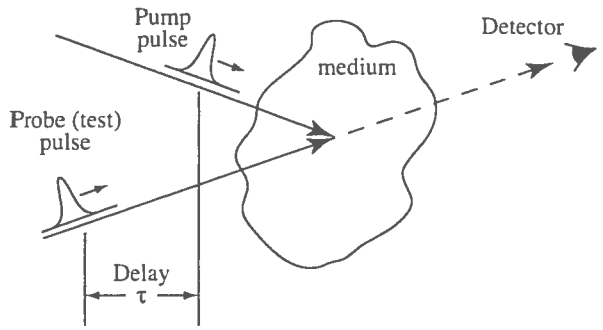

Figure 9.1 Pump–probe approach for time-resolved spectroscopy.

pulse is kept small compared to that of the pump pulse. The idea is that by detecting either the probe pulse itself, subsequent to its interaction with the sample, or by detecting some other effect induced by the interaction of the pump and probes pulse with the sample, one monitors $\Delta\mathcal{P}$ at time $t - t_0 = \tau$. By performing a series of measurements in which delay τ is varied, one maps out the full time dependence of the material response function $\Delta\mathcal{P}(\tau)$. Essentially, this is a correlation function approach, analogous to that common in pulse measurement as discussed in Chapter 3, but adapted for spectroscopic purposes. By relating the measured material response function to a microscopic model of the physical processes under investigation, one attempts to gain insight into the dynamics of these processes.

There are many different material properties that may be probed, depending, for example, on what information is desired, as well many different probing methods. A few examples of material properties and probing methods follow.

- *Transmission measurements* yield data on changes in time-resolved absorption and are often used to probe phenomena related to relaxation out of photoexcited energy states. *Reflectivity measurements* may provide similar information but are generally sensitive to changes in refractive index as well as changes in absorption.
- *Fluorescence yield* out of a state of interest may also be used to monitor the occupation of that state. In some studies the fluorescence intensity is time resolved by detecting it subsequent to a nonlinear interaction such as sum frequency generation gated by a short probe pulse.
- *Refractive index* changes may be sensed not only through reflectivity changes, but also via interferometric detection methods or via changes in the optical spectrum induced by time-varying phase. Index changes may also be observed by exploiting effects related to their spatial profile. Index changes induced by a single pump pulse typically vary radially, which may lead to focusing or deflection of a probe beam (detectable, respectively, as changes in size or position of the output probe beam). Index changes induced by a noncollinear pump pulse pair may form a spatially modulated transient grating, from which a delayed probe beam may be diffracted.
- *Dichroism* and *birefringence* refer, respectively, to anisotropic absorption and anisotropic refractive index (i.e., absorption and refractive index that depend on the polarization of the electric field). Changes in absorption (index) induced by a polarized pump pulse are often anisotropic, resulting in induced dichroism (birefringence). Measurements of time-resolved dichroism and birefringence provide information on reorientation dynamics of anisotropic molecules, for example.

- *Coherent vibrations* either of isolated molecules or of crystalline lattices may be observed via the third-order nonlinear polarization response associated with such vibrations (see Section 6.7.3). Pump–probe experiments may detect either a frequency-shifted (Raman shifted) output field or may directly resolve time-varying refractive index changes associated with the vibrations.
- *Structural information* concerning atomic-level order in crystalline samples may be probed by several different methods. For example, the transition from ordered to disordered structure in femtosecond laser-induced melting may be probed by techniques such as surface second-harmonic generation that are sensitive to order. Changes in lattice constant induced by a pump pulse may be measured by observing diffraction patterns of laser-generated x-ray or electron pulses that Bragg diffract from the crystal lattice.

Pump–probe measurements come in many flavors related to modes of detection and choice of pump and probe beams. In terms of detection, most pump–probe measurements utilize a detector with a slow response time compared to that of the dynamics of interest. In such time-integrated detection, time resolution comes about due to the ability to scan the pump–probe delay precisely. Furthermore, pump and probe pulses may be either degenerate (pulses are essentially identical, are derived directly from the same laser, and occupy the same spectral band) or nondegenerate. A representative experimental geometry for degenerate pump–probe transmission measurements is shown in Fig. 9.2. The pump and probe pulses are focused into an absorbing sample noncollinearly with controllable relative delay τ. The average power in the probe beam is measured using a time-integrating detector as a function of τ. Similar to autocorrelation measurements with repetitive pulse systems (Section 3.4.2), one commonly uses a chopper to modulate the pump beam and a lock-in amplifier to detect the component of the probe average power modulated at that frequency. In this way only the change in probe power induced by the pump beam is recorded.

In nondegenerate experiments pump and probe beams are spectrally nonoverlapping. Here the probe beam is often derived from the same laser as the pump, but frequency-

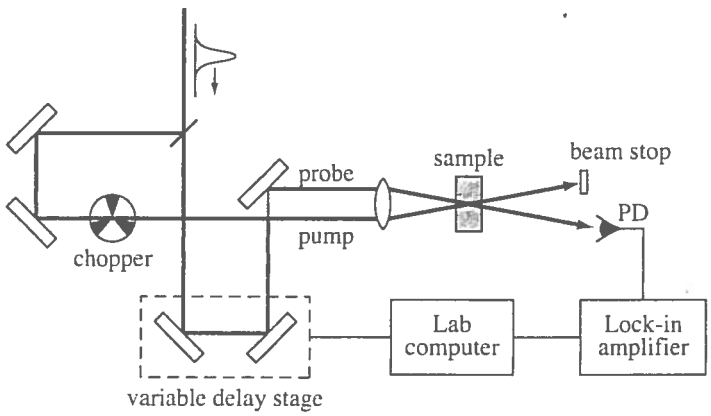

Figure 9.2 Representative experimental setup for pump–probe measurements in transmission geometry. The chopper and lock-in amplifier pull out the change in the power of the transmitted probe induced by the presence of the pump. PD, photodetector.

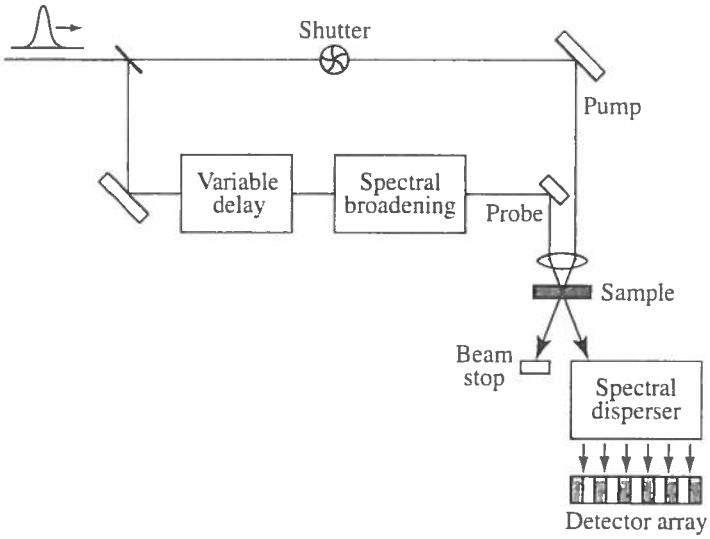

Figure 9.3 Experimental setup for spectrally resolved pump–probe measurements. To obtain differential spectra, data are collected with the shutter alternately passing and blocking the pump beam.

conversion processes are used to shift the frequency of the pump, the probe, or both. For example, the pump may lie in the visible spectrum, while the probe beam may be elsewhere in the visible, in the ultraviolet or infrared, or even in more exotic frequency regions such as terahertz or x-ray. Furthermore, the process of continuum generation (see Section 6.8) provides access to probe pulses with extremely broad frequency content. This makes possible spectrally resolved pump–probe experiments, depicted schematically in Fig. 9.3. The arrangement is similar to that for degenerate pump–probe except that prior to the sample, the probe is spectrally broadened to cover the frequency range of interest; and after passing through the sample, the probe is spectrally dispersed and then measured in parallel via a (time-integrating) photo-detector array. This gives the transmitted probe spectrum. Typically, spectra are recorded both with the pump on and with the pump blocked; subtracting these yields the differential transmission spectrum. Such differential spectra are then recorded as a function of probe delay. The resulting time- and frequency-resolved pump–probe data often provide much richer information than is possible in degenerate measurements (which provide only time resolution).

In contrast to the examples given above, some measurement schemes directly resolve the temporal profile of the probe pulse transmitted or of some other optically induced effect. Figure 9.4 shows the basic setup for experiments in which the time dependence of emitted fluorescence is measured [248]. Here a pump pulse photoexcites an absorbing sample, which then radiates fluorescence into a wide solid angle as a result of its photorelaxation processes. In conventional fluorescence techniques, the light emitted is collected and analyzed as a function of frequency to yield a (time-integrated) fluorescence spectrum. Figure 9.4 adds an ultrafast time gate activated by a delayed probe pulse to time resolve the evolution of the fluorescence spectrum. The time gating operation is typically implemented through sum frequency generation in a thin nonlinear crystal (see Section 5.5.1). Time-resolved fluorescence spectroscopy is especially well suited for tracing time-dependent energy distributions of molecules or charge carriers within an excited electronic energy manifold or band.

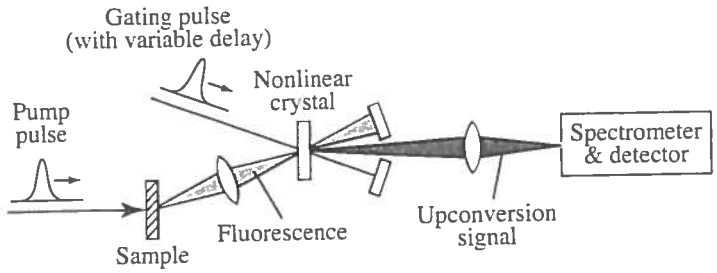

Figure 9.4 Experimental setup for time-resolved fluorescence spectroscopy.

Many other measurement schemes based on the basic concept of pump and probe are possible. A few additional examples are described later in the chapter.

Many of the topics we consider in this chapter involve resonant laser–material interactions (i.e., light is absorbed). This is in contrast to the nonresonant nonlinear interactions discussed in Chapters 5 and 6. In the following we discuss several important methods of ultrafast spectroscopy, all based on the pump–probe concept. In the course of this treatment, we sometimes illustrate measurement techniques by referring to ultrafast processes occurring in representative physical systems. However, we do not attempt to broadly survey the diverse range of physical systems that have been studied via the tools of ultrafast time-resolved spectroscopy. For detailed discussion of ultrafast processes in specific physical systems, the reader is directed to monographs such as [249,505,506] or to the proceedings of specialty conferences such as the International Conference on Ultrafast Phenomena (e.g, [507]).

The remainder of this chapter is organized as follows. In Section 9.2 we give a detailed analysis of the degenerate pump–probe measurement technique, including both induced grating and orientational relaxation phenomena. Spectrally resolved pump–probe is illustrated in Section 9.3 by referring to experiments revealing energy relaxation in both organic molecules and semiconductors. In Section 9.4 we review the quantum mechanics formalism needed for a discussion of coherent ultrashort-pulse phenomena and spectroscopy. Coherent wave packets excited in matter systems via resonant ultrashort-pulse excitation are discussed in Section 9.5; examples involving semiconductor nanostructures as well as molecules are presented. Measurement of phase relaxation phenomena is covered in Section 9.6, and coherent vibrations generated in response to nonresonant ultrashort pulse excitation are discussed in Section 9.7.

9.2 DEGENERATE PUMP–PROBE TRANSMISSION MEASUREMENTS

In this section we analyze degenerate pump–probe measurements in a transmission configuration, as sketched in Fig. 9.2. We begin with a scalar treatment useful for co-polarized pump and probe pulses.

9.2.1 Co-polarized Fields: Scalar Treatment

Denote the absorption coefficient of the sample as $\alpha(t) = \alpha_0 + \Delta\alpha(t)$, where α_0 and $\Delta\alpha(t)$ represent the static absorption and the time-dependent absorption change induced by the field, respectively. We assume that the absorption change may be expressed as the

advantage that only a single laser is required. On the other hand, ultrafast systems that provide synchronized short pulses at different optical frequencies have become common. From the analysis perspective, the use of nondegenerate pump and probe pulses gets rid of the coherent coupling artifact that was discussed in depth in Section 9.2. More important, nondegenerate measurements (using continuum probe pulses, for example) allow study of time- and frequency-resolved pump–probe data, resulting in much richer information than possible in degenerate measurements alone. In the following we adopt a case study approach in which we survey studies of ultrafast energy relaxation dynamics, first in large organic molecules in solution, specifically dye molecules, and then in the direct bandgap semiconductor GaAs. Both of these serve as model systems that were heavily investigated early in the history of femtosecond spectroscopy. Our intent is to illustrate new information that becomes available with nondegenerate and spectrally resolved measurement techniques, and in the course of this discussion, to touch upon examples of interesting ultrafast photophysics.

9.3.1 Femtosecond Pump–Probe Studies of Dye Molecules

An energy diagram relevant to the study of dye molecules is sketched in Fig. 9.11 [515]. This diagram shows the energies of the electronic ground-state and first electronic excited-state manifolds (denoted S_0 and S_1, respectively) as a function of generalized molecular coordinates Q. Q is sketched in one dimension for convenience but actually represents a multidimensional space defining the positions of the nuclei that compose the molecule. In a Born–Oppenheimer approximation picture, described mathematically in Section 9.5.2, electronic and nuclear motions are taken to be separable; for a given electronic state, energies are calculated as a function of nuclear positions, which are assumed to be clamped during the calculation. For different electronic states, minimum energy occurs at different nuclear configurations. We may understand this by recalling that it is the attraction between negatively charged electrons and positively charged nuclei that overcomes repulsive

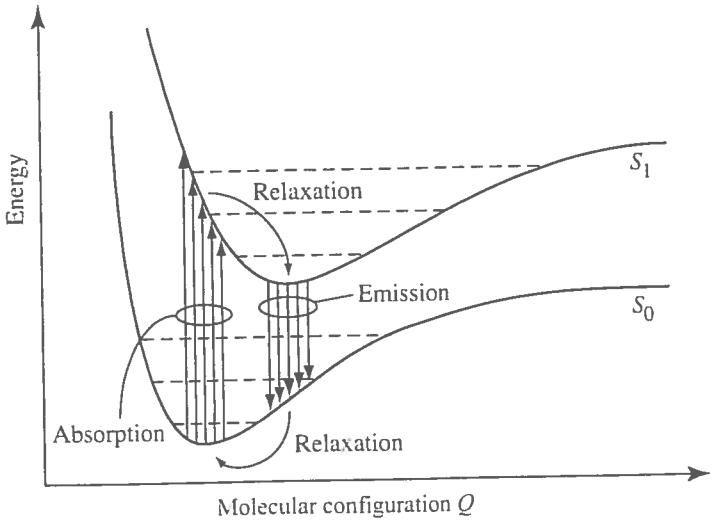

Figure 9.11 Potential energy surfaces relevant to photoexcitation and relaxation dynamics in molecules. Vibrational levels bound within the potential surfaces are depicted as dashed lines.

nuclear–nuclear forces to bind the molecule together. The result is an effective potential acting on the nuclei, which depends on the spatial distribution of the electrons relative to the nuclei and hence on the electronic wave function.

According to the Franck–Condon principle, electronic transitions occur vertically (i.e., without displacement of the nuclei). In other words, the molecular coordinates Q immediately after an electronic transition are identical to those immediately prior to the transition. This approximation, like the Born–Oppenheimer approximation of the preceding paragraph, is motivated by the much heavier mass of nuclei compared to that of electrons, which results in vibrational (nuclear) motions much slower than characteristic time scales for electron motions. Following excitation the molecule rapidly relaxes out of the initially photoexcited levels, transferring excess energy into molecular vibrations [516–518]. As a result of this vibrational relaxation process, the molecule rearranges itself to reach the lowest-energy configuration within the S_1 manifold, typically within a picosecond. On a slower time scale, other processes, such as orientational relaxation (tens to hundreds of picoseconds: see Section 9.2.2) and radiative relaxation (hundreds of picoseconds to several nanoseconds), may be observed. In the following we focus on some of the fast initial relaxation processes.

Note that for descriptions of laser operation, the dye molecule is often modeled as a four level system (see Fig. 1.5). Pumping occurs from low-energy states within the S_0 manifold (level 1) to excited states in S_1 (level 2); stimulated emission occurs from low-energy states near the bottom of S_1 (level 3) to excited states within S_0 (level 4). As discussed above, fast vibrational relaxation is responsible for taking the initially photoexcited molecule from level 2 to level 3, where it contributes to a population inversion, and then from level 3 to level 4 (subsequent to stimulated or spontaneous emission). This picture correctly predicts that the molecule's fluorescence and gain spectra are red-shifted with respect to its absorption spectrum.

Figure 9.12 shows degenerate pump–probe data for Nile blue dye in methanol, performed with pulses 70 fs in duration. These data are of interest not only because they reveal rapid

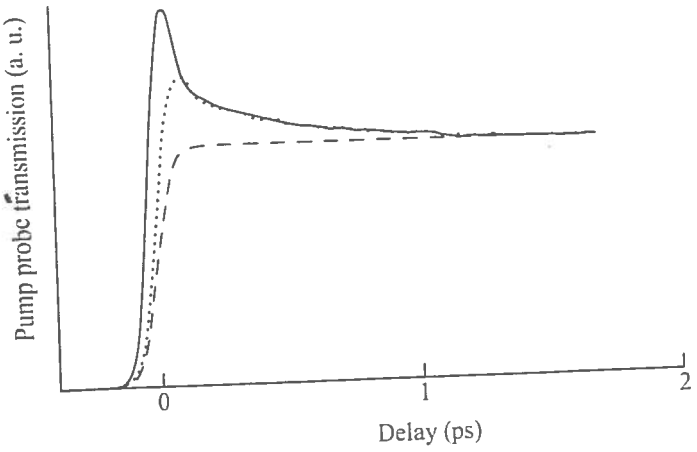

Figure 9.12 Transmission pump–probe data for Nile blue dye in methanol. Plots include the unprocessed data (solid line), data after approximate removal of coherent coupling term (dotted line), and the integral of the intensity autocorrelation (dashed line). From [516].

dynamics immediately following photoexcitation but also because they illustrate limits to the information that may be extracted from such degenerate experiments. The data show a fast rise, with strong peaking near zero delay, followed by a subpicosecond decay to a constant level. As explained previously, such degenerate pump–probe data contain contributions both from the desired absorption dynamics as well as from the coherent coupling artifact. Accordingly, the data are processed with the intent of removing the coherent coupling term, which can be accomplished at least approximately by independently measuring and then subtracting the squared electric field autocorrelation function (scaled to one-half of the $\tau = 0$ signal level). Recalling that the likelihood of absorption is proportional to the population difference $N_1 - N_2$ between initial and excited states, we may attribute the remaining bleaching signal to two mechanisms:

1. *Depopulation of the electronic ground state* S_0 (decrease in population N_1 of level 1). This effect is long-lived and recovers slowly via radiative relaxation. Over the short time window shown in Fig. 9.12, ground-state depopulation may be modeled as a step function contribution to the absorption response function. This yields a contribution proportional to the integral of the intensity autocorrelation function to the pump–probe saturation term.
2. *Introduction of population into the initially photoexcited levels in* S_1 (increase in population N_2 of level 2). This population of molecules gives rise to stimulated emission at the probe frequency, which further decreases the net absorption. This effect manifests itself as an additional signal beyond the integrated intensity autocorrelation and exhibits a rapid decay indicative of the time for molecules to relax out of the initially photoexcited states. These data may be satisfactorily fit with a biexponential absorption response, with a slower time constant of order 400 fs and a faster time constant on the order of the pulse duration.

These degenerate pump–probe data unequivocally reveal fast molecular dynamics following photoexcitation. Similar effects are seen in other dye molecules. However, such measurements are not able to reveal the dynamics after the decay out of the initially photoexcited states. In particular, neither the time required for molecules to relax to the lowest-energy states in S_1, nor the details of the relaxation process within the excited-state manifold, are revealed.

Spectrally resolved data for cresyl violet dye in solution are plotted in Fig. 9.13. In these experiments, configured as illustrated in Fig. 9.3, the sample was excited by 60-fs pump pulses centered at 618 nm, and a fiber and grating pulse compressor (see Section 6.4) was used to obtain probe pulses that were both spectrally broadened and compressed in time to 10 fs. Figure 9.13a shows a comparison of absorption spectra taken for negative delay (prior to arrival of the pump pulse) and for delay near zero (pump and probe coincide). Consistent with our earlier discussion, a prompt absorption decrease is seen in the frequency region near the pump. However, the spectrally resolved data immediately provide new information as well: The absorption change is spectrally nonuniform, comprising spectral holes both at the pump wavelength and at positions symmetrically shifted up and down in frequency from the pump. Similar effects are observed with other dye molecules, including Nile blue.

To understand these data, we must introduce the concept of vibronic transitions [515,519]. The energy surfaces introduced in connection with Fig. 9.11 refer only to an effective *potential energy* without consideration of nuclear motions (*kinetic energy*). However, nuclear

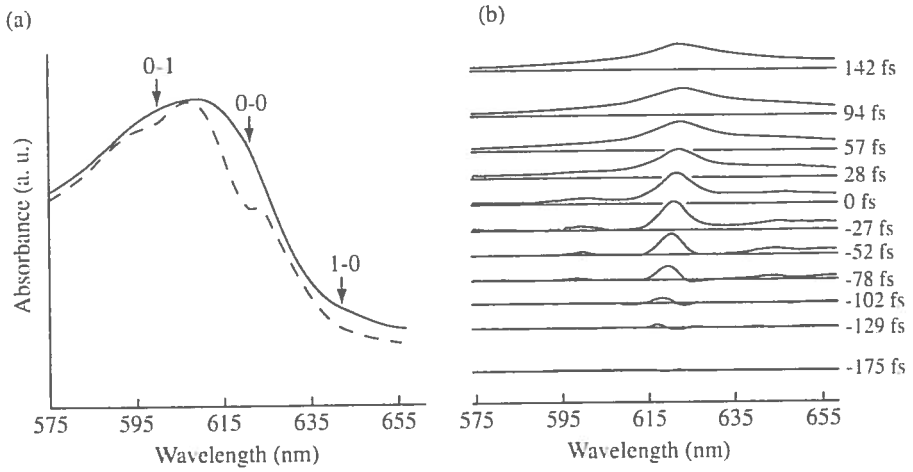

Figure 9.13 Spectrally resolved pump–probe data for cresyl violet dye in solution: (a) absorbance spectrum near zero time delay before (solid line) and after (dashed line) excitation with 60-fs pump pulse; (b) differential transmittance spectra at various relative time delays. Adapted from [517].

motions are also possible and give rise to discrete vibrational levels bound within the effective potential. Representative energy levels of such vibrational states within S_0 and S_1 are shown as dashed lines in Fig. 9.11. In a vibronic transition, absorption of a photon results in simultaneous transitions between both electronic and vibrational states. The absorption spectrum of a large dye molecule in equilibrium is strongly affected by vibronic transitions and may be written in the form [519]

$$\alpha(\omega) \sim \sum_{i,f} P_i \chi_{if} \mathcal{L}_{if}(\omega - \omega_{if}) \tag{9.31}$$

where ω_{if} is the transition frequency between the initial vibrational level in the electronic ground state and the final vibrational level in the electronic excited state; χ_{if} is the Franck–Condon factor, which quantifies the degree of spatial overlap of initial and final vibrational wave functions; P_i gives the thermal equilibrium occupation probability of the initial state; and the $\mathcal{L}_{if}$ are the line shapes of the various transitions.

The pump pulse in these experiments is resonant with the transition between the lowest vibrational levels in the S_0 and S_1 electronic states (termed the 0–0 *transition*). Thus, the prompt appearance of the central hole designated 0–0 in Fig. 9.13a results from the direct absorption process, with both depopulation of the initial state and population of the final state contributing to the bleaching. As explained in [517], the prompt replica holes are manifestations of vibronic transitions associated with a vibrational mode at about 600 cm^{-1} known from Raman scattering. In particular, the 0–1 hole is associated with the transition between the partially depopulated ground vibrational state in S_0 to the first excited vibrational level in S_1, while the 1–0 hole is associated with the transition from the thermally populated first excited vibrational level in S_0 to the partially populated ground vibrational level in S_1. Although a dye molecule has a large number of degrees of freedom and hence a large number of vibrational modes, the observation of distinct replica holes indicates that only a few modes are optically active, in the sense that their occupation numbers are altered

significantly during the optical transition. Hence, these data show that pumping with a sufficiently short pulse induces a nonequilibrium distribution of population among the vibronic levels.

The observation of spectral holes also indicates that over short time scales, dye molecules appear to be inhomogeneously broadened. The concepts of homogeneous and inhomogeneous broadening are treated in some detail later in the chapter. Briefly, by *inhomogeneous broadening* we mean that instantaneous vibronic spectra are shifted (or distorted) in a different way for different individual molecules. The widths of the spectral holes reflect the $\mathcal{L}_{if}$ line shape functions in eq. (9.31), convolved with the pump pulse spectrum. The spectral shifts and distortions responsible for inhomogeneous broadening may be explained on the basis of coupling between the few optically active modes and the large number of modes that are optically inactive. In a real space picture, these effects are related to differences in instantaneous molecular configurations in the multidimensional nuclear coordinate space. The contributions of individual molecules are not distinguished in the linear absorption spectrum, which is simply the ensemble average over the full inhomogeneous distribution, but are brought out in the spectrally resolved pump–probe.

Figure 9.13b shows a progression of differential transmission spectra recorded at various pump–probe delays. The spectral holes are observed to broaden and then merge into a smooth continuum on a time scale on the order of 100 fs. These data show that for such large molecules in solution, inhomogeneous broadening effects are short lived; individual molecules quickly lose memory of their specific initial absorption spectrum. This fast relaxation of the induced nonthermal population distribution occurs on a time scale similar to that of the fast initial decay observed in degenerate pump–probe data such as those of Fig. 9.12.

Additional interesting relaxation processes continue to occur on a variety of time scales. Temporally and spectrally resolved fluorescence measurements [518], for example, suggest that full equilibration of vibrational energy among the modes of the molecule may continue for several hundred femtoseconds. Even after the vibrational population reaches a thermal distribution, the temperature characterizing the vibrational distribution may exceed the solvent temperature significantly. Vibrational cooling in which excess vibrational energy diffuses into the solvent appears to occur on a time scale of several picoseconds [519].

9.3.2 Femtosecond Pump–Probe Studies of GaAs

Direct bandgap semiconductors such as gallium arsenide (GaAs) are of significant technological importance both in optoelectronics (diode lasers, photodetectors, etc.) and in high-speed electronics. These materials have been studied extensively via the tools of time-resolved spectroscopy, both because of fundamental interest in nonequilibrium charge carrier physics and because of practical implications for understanding and design of high-speed devices. Like large molecules, semiconductors exhibit a number of ultrafast physical processes on a variety of time scales. Reference [249] classifies the relaxation of a semiconductor excited out of thermal equilibrium by an ultrashort pulse into four temporally overlapping stages. These are summarized briefly as follows:

- *Coherent regime* ($\lesssim$ 200 fs). In this regime excitations within the semiconductor, such as optical polarization, remain in phase with each other and with the electric field of the pulse giving rise to such excitations. Processes such as carrier–carrier scattering and momentum relaxation rapidly act to disrupt (or dephase) the coherence, with characteristic time scale on the order of 200 fs or significantly faster. Ultrafast spectroscopy

methods that provide information on coherence (and loss of coherence) are discussed later in the chapter.

- *Nonthermal regime* ($\leq$ 2 ps). Excitations remaining immediately after loss of coherence (e.g., electron–hole pairs) are generally not yet thermalized: that is, the distribution of such excitations (e.g., as a function of energy) cannot yet be characterized by a temperature. Processes causing exchange of energy among carriers as well processes involving interactions between the carriers and lattice act to bring the carriers into a thermal distribution. Time scales depend on carrier densities but are typically a few hundred femtoseconds for either electrons or holes to thermalize among themselves, while a few picoseconds may be required for electrons and holes to reach a common temperature.
- *Hot carrier regime* (ca. 1–100 ps). Even after the charge carriers reach thermal distributions, they are not yet in thermal equilibrium with the crystal lattice. That is, the carrier distributions may be characterized by temperatures much higher than that of the lattice itself. Cooling of the hot carrier population, in which the carriers lose energy to the lattice, is mediated by various phonon modes of the semiconductor. The time required for carriers to cool to the lattice temperature is typically on the order of picoseconds to about 100 ps (depending, for example, on the temperature at which experiments are performed).
- *Isothermal regime* ($\geq$ 100 ps). After the carrier populations and the lattice reach equilibrium with each other (at the lattice temperature), the carrier densities are still large compared to thermal equilibrium. Finally, carriers decay via radiative and nonradiative recombination processes to restore the semiconductor to its initial state, with typical time scales ranging from a few hundred picoseconds to a few nanoseconds.

In this section we discuss a few examples of experiments that provide information on early relaxation of photoexcited carriers, primarily in the nonthermal and hot carrier regimes.

Due to the periodic crystal lattice and associated periodic potential felt by electrons moving in a semiconductor lattice, electron wave functions consist of a periodic part multiplied by a plane-wave term with wave vector $\mathbf{k}$. The energy states of the electrons are specified as a function of the wave vector or equivalently of the crystal momentum $\hbar\mathbf{k}$ [520,521]. Energy band diagrams, in which allowed electron energies are plotted as a function of wave vector, are key to understanding optical spectroscopy studies in semiconductors. A simplified schematic view of the energy band structure for GaAs is shown in Fig. 9.14 (see also [249]). The conduction band has minimum energy at $\mathbf{k} = 0$, denoted the Γ point. There are additional energy minima at symmetry points termed L and X for wave vector magnitudes at the maximum of the allowed zone; these additional minima influence both ultrafast carrier relaxation dynamics and high-field transport. There are three valence bands: the *heavy hole, light hole*, and *split-off bands*. Heavy and light hole bands have identical energy extrema at $\mathbf{k} = 0$, while the split-off band has its energy extremum also at $\mathbf{k} = 0$ but at lower energy. In undoped samples at low temperature, the valence bands are full of electrons, whereas the conduction band is empty. Therefore, photons with energy exceeding the bandgap may be absorbed, leading to generation of electrons and holes, respectively, in conduction and valence bands. The minimum bandgap for transitions from heavy and light hole bands to the conduction band is located at $\mathbf{k} = 0$ and is approximately 1.42 eV at room temperature. Note that because visible photons have wavelength on the scale of a micrometer, the wave vector (momentum) associated with a photon is small relative to the

THE JOURNAL OF PHYSICAL CHEMISTRY C

ARTICLE

pubs.acs.org/JPCC

Competitive Adsorption at the Air−Water Interface: A Second Harmonic Generation Study

Kalyanasis Sahu,[§,†,‡] Kenneth B. Eisenthal,[*,‡] and V. Faye McNeill[*,†]

[†]Department of Chemical Engineering and [‡]Department of Chemistry, Columbia University, New York, New York 10027, United States

Supporting Information

ABSTRACT: Competitive adsorption between coumarin 314 (C314) and acetonitrile at the air−water interface was studied using second harmonic generation, taking advantage of both the surface specificity and molecule selectivity of the technique. The surface concentration of C314 was selectively probed at the air−aqueous interface. As acetonitrile was added to the solution it was observed that acetonitrile displaces C314 at the interface. The experimental results are well-represented by a competitive Frumkin−Fowler−Guggenheim (cFFG) adsorption model.

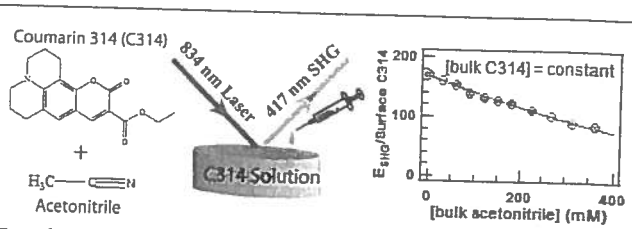

INTRODUCTION

The coexistence of surface-active organics at the air−aqueous interface changes the chemical and physical properties of the interface. This is critical for such varied processes as charge-transfer reactions in environmental systems,[1−3] personal care product design,[4−6] gas retention in bread dough,[7,8] and proper lung function.[9−11] In a complex aqueous mixture, the population of species at the interface is determined by a variety of factors including the adsorption thermodynamics for each molecule, their relative concentrations, and intermolecular interactions at the surface. Measurement of the adsorption isotherm of one component selectively in the presence of others is not straightforward. Conventional techniques like surface tension[4−12] will measure the surface excess of all components but cannot probe the surface concentration of individual components in a mixture. Interactions among molecules at the air−water interface can confound the results of such measurements.[4−6] In many cases the competitive adsorption processes are kinetically controlled and thus describe a nonequilibrium situation where the surface-bulk partitioning depends on additional factors such as the order of addition of the components.[10,13] Detection of single components is essential to understand such processes in more detail.[14−18] The second-order nonlinear optical techniques, second harmonic generation (SHG) and vibrational sum-frequency generation (VSFG), are monolayer-sensitive and provide details of molecular adsorption geometry.[19,20] They are surface-specific because second-order nonlinear processes are allowed in the asymmetric interface regions only and are forbidden in bulk. Molecular selectivity is achieved by adjusting the frequency of the incident light to match an electronic resonance (for SHG) or a vibrational resonance (for SFG). In this way, an enhancement of 3−5 orders of magnitude is obtained.[19,20]

We used second harmonic generation to study competitive adsorption between coumarin 314 (C314) and acetonitrile (Scheme 1) at the air−water interface. C314 is a slightly soluble, surface-active dye. It is an aromatic molecule containing carbonyl, ethyl ester, lactone groups, and C−N bonds that can be viewed as a model for environmental humic-like substances (HULIS).[21] The second harmonic absorption peak of C314 at the air−water interface is 419 nm.[22] The SHG signal can be strongly enhanced if the wavelength is close to a two-photon resonant with an electronic transition, in this case the $S_0 \rightarrow S_1$ transition of C314.[22] Acetonitrile is a soluble surface-active organic liquid which does not have any resonance at this wavelength. As a result, in a mixture of C314 and acetonitrile we can selectively probe the SHG response from C314 molecules in the presence of acetonitrile at the air−water interface. In this way we monitor the effect of acetonitrile on the adsorption behavior of C314 at the air−water interface. Another reason for choosing these two molecules for study is that both are nonionic and do not show strong acid−base properties in water and, hence, the ionic strength or pH of the solution is not expected to change upon varying concentration of any of the components.

The aim of this work is 2-fold: (1) to study competitive adsorption of two species with considerable affinity for the air−aqueous interface, of which C314 is slightly soluble, and acetonitrile is soluble in bulk water; (2) to demonstrate the applicability of SHG to the detailed study of surface processes in complex aqueous organic mixtures.

EXPERIMENTAL SECTION

Coumarin 314 (C314, 97%) and acetonitrile were purchased from Sigma-Aldrich and used as received. Neutral water (pH 7) of 18 MΩ/cm was used in the experiments to prepare all solutions. No additional salt or buffer was added. Experiments were done at a room temperature of 22 °C. The surface tension of the water used in these experiments was 72.1 ± 0.3 dyn/cm at that temperature.

Received: March 8, 2011
Revised: April 7, 2011
Published: April 26, 2011

ACS Publications © 2011 American Chemical Society

Scheme 1. Competitive Adsorption at the Air–Water Interface between Two Organic Molecules, Coumarin 314 (C314) and Acetonitrile[a]

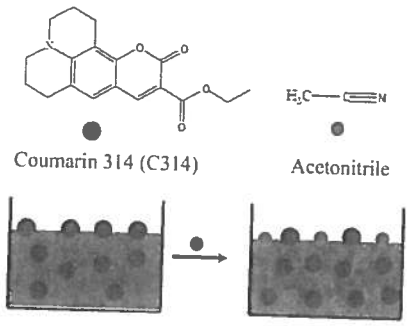

[a] Acetonitrile displaces C314 from the interface.

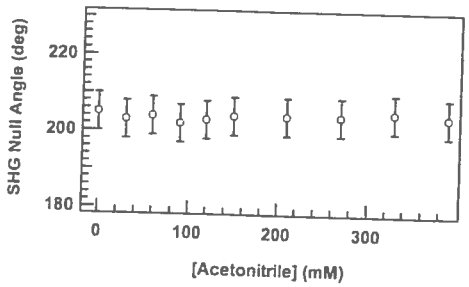

Figure 1. SHG Null angle of 14 μM C314 solution at different concentrations of acetonitrile.

C314 stock solutions were prepared by adding approximately 30 mg of C314 to 250 mL of water. The resulting mixture was sonicated for 2 h with occasional stirring and then stirred for another hour to ensure homogeneity. The excess C314 was then removed using a membrane filter with 0.45 μM diameter pores. Concentration of the stock solutions was calculated from the molar extinction coefficient (46000 $M^{-1}cm^{-1}$) at the absorption maxima (449 nm). Absorption spectra were measured using a Cary 5000 spectrophotometer. Concentration of the solution was checked to be stable for over 6 h by optical density measurements. A wait time of ~45 min was allowed for the aqueous C314 solution to reach equilibrium before collection of the SHG signal. To prepare C314–acetonitrile mixtures, the required amount of acetonitrile was injected into the C314 solution. A mixing time of ~8 min was given after each addition of acetonitrile before collecting the SHG signal. Note that subsaturation concentrations were used for both species. The C314 concentration (7–14 μM) is less than the saturation concentration (~30 μM). The surface excess of acetonitrile at the air–water interface reaches its maximum value at a bulk mole fraction of ~0.1(4.7).[23] In this study, the maximum concentration of acetonitrile used is 0.5 M.

The laser setup for SHG experiments consisted of a Nd:YVO_4 solid state laser (Spectra-physics, Millenia Vs) pumped Ti:sapphire laser (KMLab) which provides 50 fs pulses at 834 nm. The fundamental beam with energy of 2 nJ per pulse was focused to the sample interface at 70° from the surface normal. Polarization of the beam was controlled by a half-wave plate and a polarizer. A red filter is used before the sample to cut off any possible second harmonic from the fundamental laser

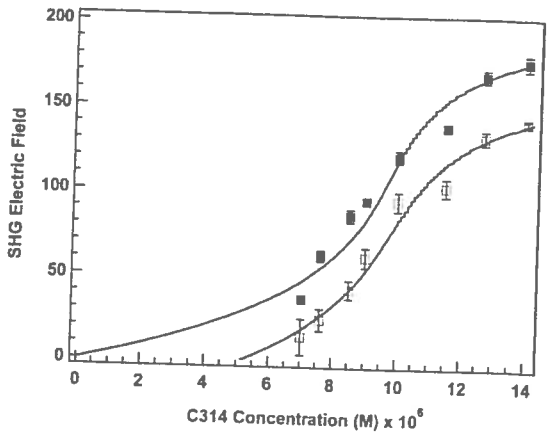

Figure 2. Adsorption isotherm of C314 in the absence (blue solid box), and in the presence (red open box) of 120 mM acetonitrile. Curves shown are from a fit using eqs 2 and 6 respectively.

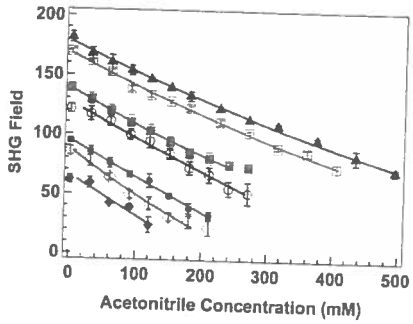

Figure 3. SHG electric field as a function of concentration of acetonitrile added to C314 solutions at varying bulk concentrations: 7.6 μM (red solid diamond), 8.5 μM (blue open diamond), 9 μM (dark red solid box), 10 μM (black open circle), 11.5 μM (dark green solid box), 12.7 μM (green open box) and 14 μM (dark blue solid triangle). Curves shown are the fit using eq 5.

impinging on optical components before it reaches the interface. From the beam reflected off the sample surface, the fundamental beam was removed with a blue pass filter and the signal at the second harmonic wavelength (417 nm) is selected by a monochromator (CVI Digikrom 240). An analyzer was placed to select the s-polarization of the signal. Our detector was composed of a PMT (Hamamatsu R4220P) and a single photon counter. For the SHG isotherm measurements, input polarization was fixed at 45° with respect to the incident plane and the s-polarized signal was detected. To measure the null angle, the analyzer was rotated to obtain the lowest signal, keeping the input polarization at 45° (Figure 1). The sample dish was on a rotating stage (Newport ESP 100 Universal motion controller/driver) to minimize local heating of the sample. SHG measurements were done at 22 °C.

RESULTS

The surface second harmonic signal from an aqueous C314 solution at a given bulk concentration of C314 decreases with addition of acetonitrile into the solution. This is clear from Figure 2 which shows a second harmonic field (square root of second harmonic signal) both in the absence and in the presence of 120 mM acetonitrile at different bulk concentrations of C314. The second harmonic field (square root of second harmonic

dx.doi.org/10.1021/jp2022083 |J. Phys. Chem. C 2011, 115, 9701–9705

signal) is proportional to the number of resonant surface species (in this case, C314) weighted by the orientation average. From null-angle measurements of the SHG light, it was found that the orientation of C314 does not change with increasing acetonitrile concentration, as expected at the low acetonitrile concentrations used here (Figure 1). Hence, SHG field is directly proportional to the number of C314 molecules present at the interface and, consequently, the plots in Figure 3 may be considered as adsorption isotherms of C314 at the air−water interface in the absence and the presence of 120 mM acetonitrile. It is clear that in the presence of acetonitrile, less C314 resides at the interface for a given bulk concentration of C314 (Scheme 1). Moreover, Figure 3 shows, in the range of conditions studied, the decrease in SH field is roughly linear with increasing acetonitrile concentration.

■ DISCUSSION

Modeling of Single Species Adsorption. The adsorption behavior for single adsorbed species can be modeled by Frumkin−Fowler−Guggenheim (FFG) isotherm which is a modification of the Langmuir isotherm incorporating lateral interaction between absorbed molecules.[24−31] The FFG equation is

$$\frac{\theta}{1-\theta}e^{-g\theta} = bc \qquad (1)$$

where θ is the fractional surface coverage of the absorbed species, b is the binding constant (adsorption equilibrium constant), c is bulk concentration, and g is a parameter representing the lateral interaction between the adsorbed species at the air−water interface. In the absence of lateral interaction ($g = 0$), the model reduces to the Langmuir equation.

The adsorption isotherm for acetonitrile was obtained from the surface tension data of aqueous acetonitrile mixtures reported by Cheong and Carr (see Supporting Information).[32] In this case, the surface coverage of acetonitrile (θ_a) is replaced by $\Gamma_a/\Gamma_{a,max}$ where Γ_a and $\Gamma_{a,max}$ are the surface excess and limiting surface excess of acetonitrile. The isotherm can be fitted with $g = 0$ (i.e., Langmuir adsorption model with no lateral interactions) and the binding constant of acetonitrile (b_a) was found to be 1.1 ± 0.3 (see Supporting Information).

For the C314, E_{SHG} is proportional to the surface coverage of C314 and, hence, we can replace θ_{C314} ($N_{C314}/N_{C314,max}$) by αE_{SHG}, where α is a constant. Rewriting eq 1 we get

$$C_{C314} = \frac{1}{b_{C314}}\frac{\alpha E_{SHG}}{1-\alpha E_{SHG}}e^{-g_{C314}\alpha E_{SHG}} \qquad (2)$$

A fit of eq 2 to the C314 adsorption isotherm (Figure 2) gives $\alpha = (4.5 \pm 0.2) \times 10^{-3}$, $b_{C314} = (1.86 \pm 0.16) \times 10^4$ and $g_{C314} = 3.4 \pm 0.2$. A positive value of g implies that attractive interactions exist between C314 molecules; however, the origin of such an interaction is not understood at this moment.

Modeling Adsorption of the Mixture of C314−Acetonitrile. A competitive Frumkin−Fowler−Guggenheim (cFFG) model is obtained from a simplified form of the generalized Frumkin−Damaskin adsorption isotherm, neglecting the size effect of the adsorbed species.[27,28] Applying it to the C314−acetonitrile system, we get

$$b_a c_a = \frac{\theta_a}{1-\theta_{C314}-\theta_a}e^{-g_a\theta_a - g_{C314,a}\theta_{C314}} \qquad (3)$$

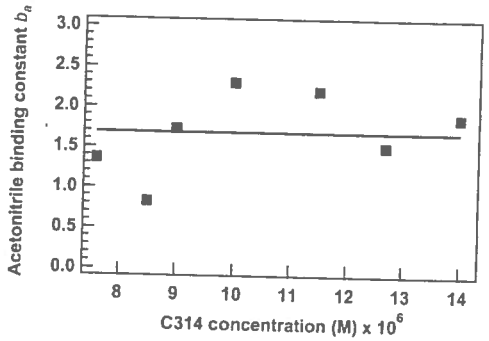

Figure 4. Dependence of acetonitrile binding constant on the C314 concentration in the C314−acetonitrile aqueous mixture. Line indicates the average binding constant of acetonitrile.

$$b_{C314}c_{C314} = \frac{\theta_{C314}}{1-\theta_{C314}-\theta_a}e^{-g_{C314}\theta_{C314} - g_{C314,a}\theta_a} \qquad (4)$$

where b_i, c_i, θ_i, g_i are equilibrium constant, bulk concentration, surface coverage, and lateral interaction, respectively, of species i (C314 or acetonitrile). The parameter $g_{C314,a}$ quantifies the lateral interaction between C314 and acetonitrile molecules at the air−water interface.

For a fixed initial C314 concentration with amount of acetonitrile varying, we can substitute: $\theta_{C314} = \alpha E^0_{SHG}$ and $\theta_a = \beta(E^0_{SHG} - E_{SHG})$ where E^0_{SHG} and E_{SHG} are the SHG field in the absence and in the presence of acetonitrile, respectively. Rewriting eq 3, we get

$$b_a c_a = \frac{\beta(E^0_{SHG} - E_{SHG})}{1-\alpha E^0_{SHG} - \beta(E^0_{SHG} - E_{SHG})}e^{-g_a\beta(E^0_{SHG} - E_{SHG}) - g_{C314,a}\alpha E^0_{SHG}} \qquad (5)$$

For 14 μM C314 bulk concentration and varying acetonitrile, using $g_a = g_{C314,a} = 0$ yields $\beta = (5 \pm 1) \times 10^{-4}$, $b_a = 1.9 \pm 0.5$, and $E^0_{SHG} = 177.72 \pm 1.63$. Changing the g values does not improve the fit. This equation describes the data for all C314 concentrations shown in Figure 3. The resulting binding constants of acetonitrile are similar (Figure 4) and nearly independent of C314 concentration. The average value of the acetonitrile binding constant was found to be 1.7 ± 0.2, similar to that calculated for solutions containing acetonitrile alone.

For a fixed acetonitrile concentration with varying C314, we may write $\theta_a = \beta(E^0_{SHG} - E_{SHG}) = \beta\Delta$ and $\theta_{C314} = \alpha(E_{SHG} + \Delta)$. Here, Δ is the decrease in SHG field due to a fraction of the surface being occupied by the acetonitrile molecules. This value is assumed to be the same for all C314 concentrations. Rewriting eq 4, we get

$$b_{C314}c_{C314} = \frac{\alpha(E_{SHG} + \Delta)}{1-\alpha(E_{SHG} + \Delta) - \beta\Delta}e^{-g_{C314}\alpha(E_{SHG} + \Delta) - g_{C314,a}\beta\Delta} \qquad (6)$$

For 120 mM acetonitrile and concentration of C314 varying using the values $g_{C314,a} = 0$, $\alpha = 4.5 \times 10^{-3}$, and $\beta = 5 \times 10^{-4}$, fit of eq 6 to the C314 desorption data in Figure 3 results $b_{C314} = (1.95 \pm 0.1) \times 10^4$, $\Delta = 33 \pm 4$, and $g_{C314} = 3.35 \pm 0.08$. This implies that addition of acetonitrile does not change the lateral interaction between the C314 molecules and no lateral interaction is found between adsorbed C314 and acetonitrile molecules.

dx.doi.org/10.1021/jp2022083 J. Phys. Chem. C 2011, 115, 9701–9705

In summary, all the experimental results are well-described by the FFG model using a similar set of fit parameters which describe the surface−bulk partitioning of each species in isolation. This suggests that the presence of acetonitrile at the surface does not affect the adsorption free energy of C314, and vice versa, under the conditions studied. This is consistent with a lack of strong intermolecular interactions between C314 and acetonitrile molecules ($g = 0$) at the surface and invariance of molecular reorientation of C314 with acetonitrile addition.

SUMMARY

We have shown that the competitive adsorption of C314 and acetonitrile at the air−aqueous interface is well-described by the FFG adsorption model. This work demonstrates the applicability of second harmonic generation to study the adsorption behavior of individual components to the air−water interface in the presence of other surface-active agents. This capability will be particularly valuable for studying the surface−bulk partitioning of organic species in complex environmentally and biologically relevant aqueous systems. For example, measurement of the surface partitioning and interface-specific properties of polycyclic aromatic hydrocarbons, humic and fulvic acids, and HULIS in complex mixtures typical of natural waters and aqueous atmospheric aerosols can elucidate the mechanisms and efficiency (and thus environmental significance) of photosensitized reactions at the air−aqueous interface.[1−3]

ASSOCIATED CONTENT

Supporting Information. Calculation of surface equilibrium constant of acetonitrile and waiting time selection for SHG signal from aqueous C314 solution. This material is available free of charge via the Internet at http://pubs.acs.org.

AUTHOR INFORMATION

Corresponding Author

*Email: vfm2103@columbia.edu, kbe1@columbia.edu.

Present Addresses

§Current affiliation: Department of Chemistry and Biochemistry, University of South Carolina, Columbia, SC, 29208.

ACKNOWLEDGMENT

V.F.M. acknowledges the NASA Tropospheric Chemistry program (Grant #NNX09AF26G) for funding. K.B.E. acknowledges NSF Division of Chemistry, DOE Office of Basic Energy Sciences, and DTRA (Grant #W911NF-07-1-0116) for support.

REFERENCES

(1) Stemmler, K.; Ndour, M.; Elshorbany, Y.; Kleffmann, J.; D'Anna, B.; George, C.; Bohn, B.; Ammann, M. Light induced conversion of nitrogen dioxide into nitrous acid on submicron humic acid aerosol. *Atmos. Chem. Phys.* **2007**, *7*, 4237–4248.

(2) Stemmler, K.; Ammann, M.; Donders, C.; Kleffmann, J.; George, C. Photosensitized reduction of nitrogen dioxide on humic acid as a source of nitrous acid. *Nature* **2006**, *440*, 195–198.

(3) Ammann, M.; Rossler, E.; Strekowski, R.; George, C. Nitrogen dioxide multiphase chemistry: Uptake kinetics on aqueous solutions containing phenolic compounds. *Phys. Chem. Chem. Phys.* **2005**, *7*, 2513–2518.

(4) Jean, B.; Lee, L. Noninteracting versus interacting poly(*N*-isopropylacrylamide)-surfactant mixtures at the air-water interface. *J. Phys. Chem. B* **2005**, *109*, 5162–5167.

(5) Chari, K.; Young-Soo, S.; Sushil, S. Competitive adsorption at the air-water interface from a self-assembling polymer-surfactant mixture. *J. Phys. Chem. B* **2004**, *108*, 11442–11446.

(6) Penfold, J.; Thomas, R. K.; Taylor, D. J. F. Polyelectrolyte/surfactant mixtures at the air−solution interface. *Curr. Opin. Colloid Interface Sci.* **2006**, *11*, 337–344.

(7) Keller, R. C. A.; Orsel, R.; Hamer, R. J. Competitive adsorption behavior of wheat flour components and emulsifier at an air-water interface. *J. Cereal Sci.* **1997**, *25*, 175–183.

(8) Mackie, A. R.; Gunning, A. P.; Wilde, P. J.; Morris, V. J. Competitive displacement of β-lactoglobulin from the air/water interface by sodium dodecyl sulfate. *Langmuir* **2000**, *16*, 8176–8181.

(9) Kim, S. H.; Franses, E. I. Competitive adsorption of fibrinogen and dipalmitoylphosphatidylcholine at the air/aqueous interface. *J. Colloid Interface Sci.* **2006**, *295*, 84–92.

(10) Stenger, P. C.; Isbell, S. G.; Hillaire, D. S.; Zasadzinski, J. A. Rediscovering the Schulze-Hardy rule in competitive adsorption to an air-water interface. *Langmuir* **2009**, *25*, 10045.

(11) McLoughlin, D.; Langevin, D. Surface complexation of DNA with a cationic surfactant. *Colloids Surf., A* **2004**, *250*, 79–87.

(12) Henning, S.; Rosenørn, T.; D'Anna, B.; Gola, A. A.; Svenningsson, B.; Bilde, M. Cloud droplet activation and surface tension of mixtures of slightly soluble organics and inorganic salt. *Atmos. Chem. Phys.* **2005**, *5*, 575–582.

(13) Tronson, R.; Ashokkumar, M.; Grieser, F. Multibubble sonoluminescence from aqueous solutions containing mixtures of surface active solutes. *J. Phys. Chem. B* **2003**, *107*, 7307–7311.

(14) Voss, L. F.; Hadad, C. M.; Allen, H. C. Competition between atmospherically relevant fatty acid monolayers at the air/water interface. *J. Phys. Chem. B* **2006**, *110*, 19487–19490.

(15) Voss, L. F.; Bazerbashi, M. F.; Beekman, C. P.; Hadad, C. M.; Allen, H. C. Oxidation of oleic acid at air/liquid interfaces. *J. Geophys. Res.* **2007**, *112*, D06209.

(16) Ma, G.; Allen, H. C. Condensing effect of palmitic acid on DPPC in mixed Langmuir monolayers. *Langmuir* **2007**, *23*, 589–597.

(17) Harper, K. L.; Allen, H. C. Competition between DPPC and SDS at the air-aqueous interface. *Langmuir* **2007**, *23*, 8925–8931.

(18) Henry, M. C.; Yang, Y.; Pizzolatto, R. L.; Messmer, M. C. Competitive Adsorption of 2,4,7,9-tertramethyl-5-decyn-4,7-diol and linear alkane surfactants at the air/water interface. *Langmuir* **2003**, *19*, 2592–2598.

(19) Shen, Y. R. Surfaces probed by nonlinear optics. *Surf. Sci.* **1994**, *299*, 551–562.

(20) Eisenthal, K. B. Liquid interfaces probed by second-harmonic and sum-frequency spectroscopy. *Chem. Rev.* **1996**, *96*, 1343–1360.

(21) Graber, E. R.; Rudich, Y. Atmospheric HULIS: How humic-like are they? A comprehensive and critical review. *Atmos. Chem. Phys.* **2006**, *6*, 729–753.

(22) Zimdars, D.; Eisenthal, K. B. Static and dynamic solvation at the air/water interface. *J. Phys. Chem. B* **2001**, *105*, 3993–4002.

(23) Rao, Y.; Turro, N. J.; Eisenthal, K. B. Water structure at air/acetonitrile aqueous solution interfaces. *J. Phys. Chem. C* **2009**, *113*, 14384–14389.

(24) Adamson, A. W. *Physical Chemistry of Surfaces*, 5th ed.; Wiley: New York, 1990.

(25) Aranovich, G. L.; Donohue, M. D. Adsorption Compression: An Important New Aspect of Adsorption Behavior and Capillarity. *Langmuir* **2003**, *19*, 2722–2735.

(26) Aranovich, G. L.; Wetzel, T. E.; Donohue, M. D. Adsorption Behavior of Repulsive Molecules. *J. Phys. Chem. B* **2005**, *109*, 10189–10193.

(27) Wuestneck, R.; Miller, R.; Kriwanek, J.; Holzbauer, H.-R. Quantification of Synergistic Interaction between Different Surfactants Using a Generalized Frumkin-Damaskin Adsorption Isotherm. *Langmuir* **1994**, *10*, 3738–3742.

(28) Wuestneck, R.; Fiedler, H.; Miller, R.; Haage, K. Surface Chemical Characterization of Maleic Acid Mono[2-(4-alkylpiperazinyl)ethyl esters]. 2. pH-Dependent Adsorption Behavior of an Amholytic Surfactant. *Langmuir* **1994**, *10*, 3966–3971.

(29) Al-Abadleh, H. A.; Mifflin, A. L.; Bertin, P. A.; Nguyen, S. T.; Geiger, F. M. Control of Carboxylic Acid and Ester Groups on Chromium (VI) Binding to Functionalized Silica/Water Interfaces Studied by Second Harmonic Generation. *J. Phys. Chem. B* **2005**, *109*, 9691–9702.

(30) Fedoseeva, M.; Fita, P.; Punzi, A.; Vauthey, E. Salt Effect on the Formation of Dye Aggregates at Liquid/Liquid Interfaces Studied by Time-Resolved Surface Second Harmonic Generation. *J. Phys. Chem. C* **2010**, *114*, 13774–13781.

(31) Petersen, P. B.; Saykally, R. J. Probing the Interfacial Structure of Aqueous Electrolytes with Femtosecond Second Harmonic Generation Spectroscopy. *J. Phys. Chem. B* **2006**, *110* (29), 14060–14073.

(32) Cheong, W. J.; Carr, P. W. The Surface Tension of Mixtures of Methanol, Acetonitrile, Tetrahydrofuran, Isopropanol, Tertiary Butanol, and Dimethyl-Sulfoxide with Water at 25 °C. *J. Liq. Chromatogr. Relat. Technol.* **1987**, *10* (4), 561–581.

dx.doi.org/10.1021/jp2022083 |*J. Phys. Chem. C* 2011, 115, 9701–9705